Fast Numerical Modeling of Propeller–Wing Aerodynamic Interactions

Nederlof, R.; Goyal, J.; Sinnige, T.; Ragni, D.; Veldhuis, L.L.M.

Fast Numerical Modeling of Propeller–Wing Aerodynamic Interactions

Robert Nederlof,* Jatinder Goyal,† Tomas Sinnige,‡
Daniele Ragni,§ and Leo L. M. Veldhuis¶
Delft University of Technology, 2629 HS Delft, The Netherlands

https://doi.org/10.2514/1.J064764

This paper presents an improved approach for fast numerical modeling of the mutual aerodynamic interactions between a wing and tractor propellers for preliminary design purposes. Vortex methods are used to model the propeller and wing aerodynamic performance. The blade element momentum (BEM) method, which is used to model the propeller performance, is extended to allow for a nonuniform inflow field, such that the upstream effects of the wing can be included in the propeller performance modeling. The circulation distribution over the propeller blades is then used in the slipstream tube model (STM) to determine the time-averaged propeller slipstream velocities. Finally, an improved vortex lattice method (VLM) is used to model the wing's spanwise lift distribution. The method includes an often overlooked correction for the finite slipstream dimensions experienced by the wing segments, in both vertical extent and spanwise extent. This physics-based correction, based on the image vortex technique, partially offsets the large discrepancies in the lift augmentation found in previous low-order numerical analyses of propeller–wing interactions, while keeping the analysis routine computationally very cheap. The BEM and STM are validated against experimental data, while the VLM and complete propeller–wing system are validated against high-fidelity numerical data, confirming the accuracy of the used models. Discrepancies are found in regions or operating conditions where viscosity becomes more relevant, such as separated flows. The numerical model derived in this paper can be used for a quick and accurate first-order estimation of the aerodynamic performance of new conceptual distributed propeller aircraft.

Nomenclature

a	=	axial induction factor (blade element momentum), -
a'	=	tangential induction factor (blade element momentum), -
B	=	number of propeller blades, -
b	=	wing span, m
$b_{i,j}$	=	y-distance in the slipstream tube model, m
C_D	=	3D drag coefficient, -
C_d	=	sectional drag coefficient; $d/[(1/2)\rho V_\infty^2 c]$, -
C_L	=	3D lift coefficient, -
C_l	=	sectional lift coefficient; $l/[(1/2)\rho V_\infty^2 c]$, -
C_P	=	propeller power coefficient; $P/(\rho n^3 D_p^5)$, -
C_T	=	propeller thrust coefficient; $T/(\rho n^2 D_p^4)$, -
c	=	chord, m
$c_{i,j}$	=	z-distance in the slipstream tube model, m
D	=	drag force, N
D_p	=	propeller diameter, m
d	=	sectional drag, N/m
db	=	vector along bound vortex filament (vortex lattice method), m
dl	=	vector along vortex filament (slipstream tube model), m
e	=	unit vector along vortex filament (slipstream tube model), -
F	=	aerodynamic influence coefficient matrix, 1/m
F	=	resultant force vector at bound vortex, N
G	=	aerodynamic correction matrix, 1/m
h	=	2D slipstream height, m
J	=	propeller advance ratio; $V_\infty/(nD_p)$, -
K	=	2D correction factor, -
L	=	lift force, N
l	=	sectional lift, N/m
M	=	total number of azimuthal sections (slipstream tube model), -
M	=	total number of streams (vortex lattice method), -
m	=	index for stream in the 2D image technique, -
N	=	total number of radial sections (slipstream tube model), -
n	=	propeller rotational speed, Hz
P	=	propeller power, W
Q	=	reference point in the slipstream, -
q	=	dynamic pressure, Pa
R	=	propeller radius, m
r	=	radial coordinate, m
r_Q	=	position vector from vortex filament to Q, m
s	=	index for stream in the 2D image technique, -
T	=	propeller thrust, N
T_C	=	thrust coefficient; $T/(\rho V_\infty^2 D_p^2)$, -
V	=	velocity component, m/s
V	=	velocity vector, m/s
v	=	downwash velocity, m/s
x	=	axial (streamwise) coordinate, m
y	=	vertical coordinate, m
z	=	spanwise coordinate, m
α	=	angle of attack, deg
α_m	=	image strength for stream m, -
β	=	blade pitch angle, deg
β_m	=	opposite image strength for stream m, -
Γ	=	circulation, m²/s
γ	=	distributed vorticity, m/s
ϵ	=	image strength factor; $(\mu^2 - 1)/(\mu^2 + 1)$, -
λ	=	taper ratio, -
μ	=	velocity ratio; V_j/V_∞, -
ρ	=	air density, kg/m³
φ	=	circumferential propeller position, rad
ω	=	propeller rotational speed, rad/s

Subscripts

$0.7R$	=	at 70% of the blade radius
a	=	axial
b	=	bound (vortex)
eff	=	effective (velocity)
ex	=	experimental
i	=	induced
j	=	jet
n	=	normal
p	=	propeller
t	=	tangential
w	=	wing
∞	=	freestream

I. Introduction

THE need for more sustainable aviation drives future aircraft designs to use propellers, owing to their high propulsive efficiency. These designs often feature multiple smaller engines that are distributed over the aircraft. Each of these engines can be used to drive a propeller, which contributes to generating the required thrust. At the same time, the beneficial propeller–wing interaction can lead to a further improvement of the aircraft's performance [1]. These so-called distributed propeller (DP) concepts offer potential benefits, such as reduced takeoff and landing capabilities due to the increased lift augmentation caused by the multiple propeller slipstreams compared to a conventional propeller aircraft. The NASA X-57 Maxwell [2] and the Electra EL-2 Goldfinch [3] are well-known examples of such DP concepts.

In order to turn the exciting outlook of these innovative aircraft into reality, the close coupling between the propellers and the airframe needs to be exploited. This requires a solid understanding and analysis or modeling capability of propeller–wing interactions. Such interactions have been studied for over a century. Starting with the pioneering work by Prandtl [4], various researchers have investigated the topic using an experimental approach [5–7]. Recent studies have focused on wingtip-mounted propellers, which have proven to lower the induced drag of the wing significantly [8–12]. The emergence of new radical aircraft designs also led to the further exploration of propeller–airframe interactions for unconventional configurations [13–15]. To have a more thorough understanding of the fundamental mutual interaction between the propeller and other aircraft components, numerical methods are often employed to analyze complex (distributed) propeller aircraft designs. In the past, simple numerical methods were used to estimate the effect of the propeller on the wing [16,17]. With the increasingly more powerful computers and the advancements in the field of CFD, many studies focus on quantifying specific aerodynamic interaction phenomena of propeller–wing configurations using Reynolds-averaged Navier–Stokes (RANS) simulations [18–22].

However, these high-fidelity simulations often focus on a specific geometry for which the interaction effects are quantified. With the increasing interaction between the propeller and airframe for the new DP aircraft concepts, the initial design phase should already account for the interaction effects in the first place [23–25]. In this way, the optimal placement of the propellers and associated wing design can be found iteratively. The increased design freedom also means that the number of variables rapidly increases, and CFD methods become too computationally expensive to analyze all possible configurations. Due to the low computational cost of vortex-based methods, they are an attractive way of analyzing the propeller–wing interaction from a lower-order perspective. It is therefore important to make these numerical tools as accurate as possible.

Previous work has led to the development of various models of propeller–wing interactions with different types of singularity methods (lifting-line [LL] method, vortex lattice method [VLM], and 3D-panel method). However, these tools are often used to model the propeller performance and wing performance separately. Most studies that use these low-order tools simply superimpose the propeller-induced velocities onto the wing vortex system to quantify the change in wing performance [26]. Such models are referred to as single interaction mode (SIM) [7]. In reality, there is a mutual interaction between the propeller and the wing that alters the performance of both components. From the experiments conducted by Sinnige et al. [9,10], it is concluded that the influence of the wing on the propeller integral performance is limited in a tractor configuration for small angles of attack. However, even a small change in propeller performance could reduce the propulsive efficiency, influencing the complete aircraft design [24,27]. A numerical model, where the performance of the wing influences the propeller and vice versa, is denoted as a full interaction mode (FIM) [7].

Although the integrated performance (thrust and torque) may not be modified much, the distribution over the disk is, and that also affects the interaction with the wing. Due to the change in wing performance caused by the propeller–wing interaction, the propeller should be operated at a different thrust condition since the thrust requirement of the complete aircraft changes. This means that the propeller could be redesigned to improve the propulsive efficiency further. This iterative aspect was highlighted in the recent work by Cole et al. [28], where an outboard-up rotating propeller located close to the wing root turned out to be the most efficient layout for a particular set of design variables, which highlights the need for the more thorough analysis of the complete design space, including the mutual interaction.

Recent numerical work has focused on the modeling of propeller–wing interactions using midfidelity vortex methods, such as free-wake panel methods [29] or vortex particle methods [30]. These are computationally cheaper than RANS simulations, since they do not require the meshing of the complete domain. Furthermore, they are easily coupled with existing lower-order methods like an LL or VLM. With these methods, more unsteady and viscous effects can be captured. However, the computational time of a free-wake panel simulation is still about a CPU hour, depending on the mesh quality required [28]. Similar run times are observed for the commercial free-wake panel solver Flightstream® [31].

For initial aircraft design studies, only the time-averaged propeller–wing effects are important to consider [24]. To understand the sensitivity and dependence of different design parameters and their effect on the change in aircraft performance, more rapid tools are needed considering the large number of possible configurations. So, there is a need for the reliable and fast analysis of the mutual interaction between propeller and wing to explore the full design space for new DP aircraft designs. Unfortunately, in many conventional low-order potential flow tools, using fixed-wake vortex panel methods, there is a significant overprediction in wing lift due to the propeller-induced velocities. This is often attributed to limitations in the modeling capabilities of the potential flow approach itself [32–35]. This could lead to incorrect propeller–wing interaction estimations and therefore overoptimistic DP aircraft designs.

This paper describes the improvement of existing low-order numerical propeller and wing performance modeling techniques. Especially for the modeling of the slipstream–wing interaction, multiple physics-based corrections are implemented, such that the accuracy of the spanwise lift distribution is improved significantly. These existing approaches, based on the image vortex technique, are refined and further improved to allow for more general layouts of the propeller–wing system. The proper combination of the separate models leads to a further improvement of the capabilities to capture the mutual propeller–wing interactions in an accurate way, such that the initial aircraft design process can be improved for new radical designs. At the same time, the computational cost of the complete analysis loop remains very low, allowing for the analysis of the whole design space. The different improved numerical models are validated individually against experimental and high-fidelity data. Furthermore, the complete framework consisting of the different models is validated using propeller–wing performance data.

II. Limitations of Low-Order Potential Flow Tools

Propeller–wing interaction effects can be modeled using low-order potential flow tools, like an LL or VLM approach. In these modeling approaches, the flowfield of the propeller and wing separately can be superimposed into a single flow domain [36]. When excluding the wing-induced velocities, the wing segments outside of the slipstream

will experience the freestream velocity as incoming velocity, while the wing segments inside the slipstream will experience a changed inflow field due to the propeller-induced velocities. However, when considering the (predescribed) fixed wake modeling of the propeller slipstream, there is no deformation due to the presence of the wing, and therefore the propeller-induced velocities inside the slipstream are effectively inaccurate [37]. When using an LL or VLM model for the performance estimation of an isolated wing, the freestream velocity is considered to be uniform and extending from "+" to "−" infinity around each wing segment. When including the interaction between the slipstream and the wing, the propeller-induced velocities are often simply added to the system of equations of the LL or VLM as if this velocity component also extends from "+" to "−" infinity for each spanwise section, which leads to an overestimation of the lift augmentation [38–41]. This assumption becomes most clear when focusing on the axial velocity at each 2D wing segment.

In the LL or VLM approach, the propeller-induced velocities are assessed at the collocation point(s) of each spanwise wing segment. When only considering the induced velocity V_i at this point, it is as if this wing segment is submerged in a jet with a single velocity. Therefore, two potential flow effects are not properly captured for wing segments inside the propeller slipstream. Firstly, if this jet-like simplification is used, the jet velocity is just simply added to the system of equations, as if this jet is infinitely high in front of the wing segment, as is the case for an undisturbed freestream analysis (see Fig. 1a). The 2D airfoil performance is then modeled by considering the segments to be in uniform flows with velocities V_j and V_∞ for sections inside and outside the slipstream, respectively. However, the finite height of the jet influences the change in aerodynamic performance. An airfoil immersed in a slipstream with jet velocity V_j and finite height h will experience less lift augmentation than an airfoil with freestream velocity V_j or, in other words, a jet with infinite height [38]. In the most limiting case, when the jet height approaches zero, the lift augmentation would also be zero, and the freestream velocity is effectively experienced by the wing segment. To satisfy the potential flow boundary conditions at the slipstream edge, a correction is needed, such that the effect of the finite height is taken into account. This is done using an image vortex technique, originally derived in the study by Ting and Liu [38].

Secondly, the complete vertical velocity profile inside the slipstream will have an influence on the aerodynamics of the wing segments. If the velocity at the control point is much lower or higher than the effective slipstream velocity, there can be an under- or overestimation of the lift augmentation (see Fig. 1b). This problem could be partially solved by assuming an equivalent jet velocity, which generates the same lift augmentation as the nonuniform velocity profile. However, determining such equivalent jet velocity would be nontrivial since the effect of the nonuniform velocity profile needs to be known a priori. The method of images used for a 2D airfoil submerged in a jet can be extended to capture the effect of the nonuniform velocity profile on the airfoil aerodynamic performance [39]. By taking multiple smaller jets with different velocities, a continuous velocity profile can be approximated.

Not accounting for the finite dimensions of the propeller slipstream in the potential flow analysis, using fixed vortex wake structures, will lead to an overestimation of the lift augmentation of the
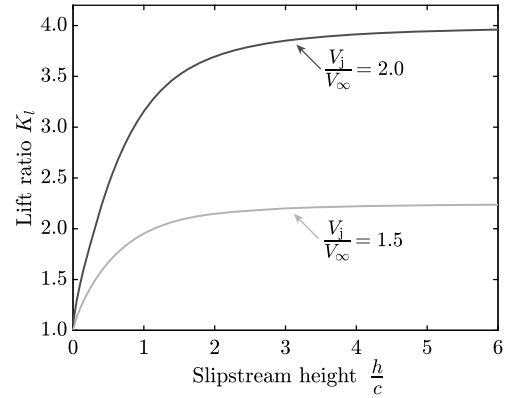

Fig. 2 Lift augmentation ratio (K_l) variation for two velocity ratios (derived from [42]).

wing caused by the slipstream [40,41], especially for small jet heights. When the jet is infinitely high, it is as if the airfoil experiences a different freestream velocity. For an airfoil in such a jet, the sectional lift l_j will scale with the velocity ratio V_j/V_∞ squared compared to the no-jet case (l_∞). However, when the jet height reduces, the lift augmentation is lowered compared to this infinite case. Examples of the lift ratio ($K_l = l_j/l_\infty$) as a function of the normalized jet height are presented for two different velocity ratios in Fig. 2. For large values of h/c, the lift ratio converged toward the square of the velocity ratio. However, for smaller jet heights, this lift ratio is reduced. Especially when the h/c is below 2, there is a significant reduction in the lift augmentation. For conventional turboprop aircraft, typical values of the propeller diameter to chord ratio (D_p/c) are around 2, meaning that the maximum value of h/c is around 2 at the center of the propeller, while it decreases toward the edges of the propeller. The effect of the limited jet height on the wing lift augmentation becomes even more important for the new DP concepts since the propeller diameter is much reduced compared to conventional turboprop aircraft, leading to smaller values of h/c, assuming a similar wing as for the conventional turboprop.

So, the finiteness and nonuniformity of the slipstream alter the 2D airfoil performance of the wing segments submerged in the slipstream. When modeling the 3D wing performance using an LL or VLM approach, only correcting the 2D airfoil performance of the wing segments inside the slipstream will not directly alter the performance of neighboring segments, only indirectly due to the induced downwash generated by these segments. However, the finite slipstream dimension in the spanwise direction also will alter the lift augmentation of the complete wing. Therefore, not only the 2D airfoil performance of each wing segment needs to be corrected for the local finite jet height. Additionally, the 3D wing performance needs to be corrected for the spanwise extent of the jet. A schematic representation of the spanwise variation in the axial velocity is shown in Fig. 3. The approach with a simplified jet-like representation has been considered by different studies in the past by including the image vortex technique [39,42,43]. In the present paper, these methods are extended to more general cases, including variable velocity profiles in both the spanwise and vertical
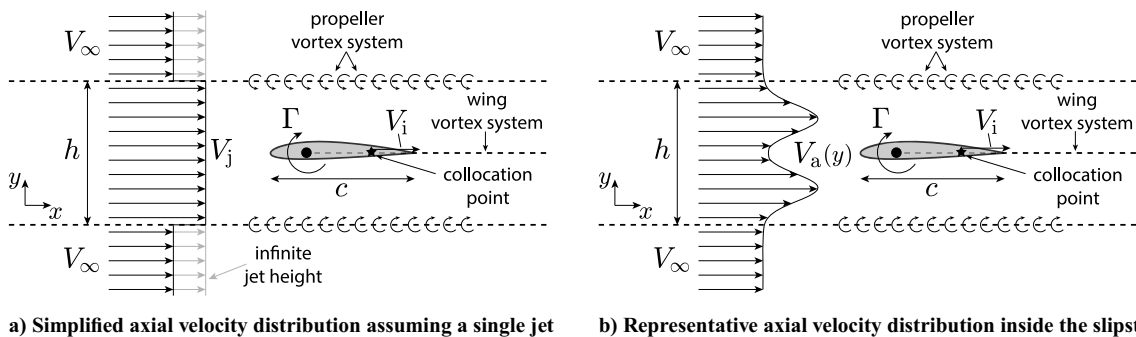

a) Simplified axial velocity distribution assuming a single jet **b) Representative axial velocity distribution inside the slipstream**

Fig. 1 Submerged 2D wing segment with a simplified and representative axial velocity profile.
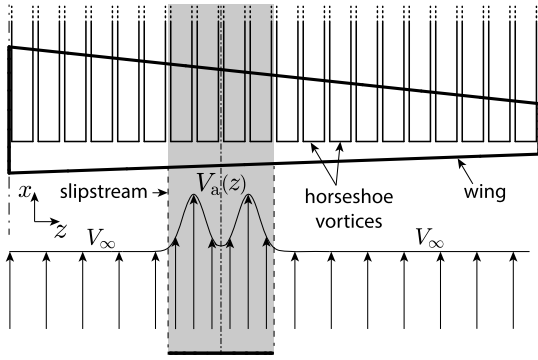
Fig. 3   Propeller–wing system with a representative axial velocity distribution in the spanwise direction.

extent of the slipstream. This is done by making use of a numerical approach as opposed to analytical solutions, which were sought for in the past due to the lack of powerful computers [36].

III.   Numerical Methods

The improved modeling of the propeller–wing interactions is presented in this section. The different submodels are introduced separately, after which their coupling is discussed. First, the propeller aerodynamics is modeled by an ordinary blade element momentum (BEM) model, which is discussed in Sec. III.A. The BEM is able to account for nonuniform (NU) inflow conditions at the propeller disk, caused by possible propeller inflow angles or generated by the wing vortex system. Once the propeller performance is known, the slipstream is modeled using the slipstream tube model (STM), which is a time-averaged vortex model to obtain the induced velocities inside the slipstream, as discussed in Sec. III.B. These induced velocities are then superimposed in a VLM to get the wing's aerodynamic performance. This VLM is extended to account for the finite slipstream effects, which are discussed in Sec. III.C. The induced velocities of the wing vortex system can be used to recalculate an upstream inflow field of the propeller to reiterate the calculations. The modeling process is schematically shown in Fig. 4.

A.   Propeller Performance Modeling

The BEM model is a commonly used tool to analyze propeller performance since it can provide accurate and fast results based on the geometry of the propeller blades. BEM methods are used extensively in the low-order modeling of propellers and have proven to give accurate results [44–47]. The BEM model used in this study was based on [48] and further improved for a wider range of operating conditions [49]. The 2D airfoil polar data were obtained using RFOIL [50], which includes a correction for the centrifugal pumping (Coriolis) effects compared to XFOIL [51]. The circulation distribution over the propeller blades is then used in the STM to calculate the slipstream-induced velocities. The circulation at each radial segment is calculated using the local lift coefficient C_l, the local chord c, and the local velocity at each radial segment (V_{eff}), which includes the axial and tangential induction factors a and a', respectively:

$$\Gamma_p(r) = \frac{V_{\text{eff}}\, c\, C_l}{2} \qquad V_{\text{eff}} = \sqrt{(V_\infty(1+a))^2 + (\omega r(1-a'))^2} \quad (1)$$
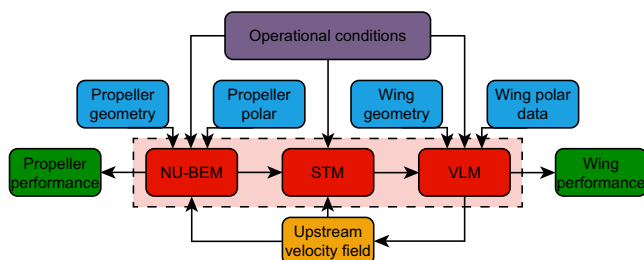

Fig. 4   Flowchart for the propeller–wing interaction modeling.

To implement the effect of a nonuniform inflow field at the propeller disk, the BEM is adapted to allow for the discretization of the propeller disk in the azimuthal direction, such that the loading can vary depending on the blade position. This means that the blade element part of the analyses is altered to account for a different effective velocity at the blade sections compared to the uniform inflow case. The associated varying loading results in a change in induction in the azimuthal direction, affecting the momentum theory part of the BEM model [52,53]. Note that in the BEM there is no interaction between the radial segments; hence, there will be no change in sectional blade performance due to the nonuniformity along the radius for each azimuthal angle. To simplify the analysis, the BEM is solved for each azimuthal angle as if the whole disk would experience the flowfield that the blades encounter at that azimuthal position. The true response of the propeller to the nonuniform inflow field is not instantaneous, meaning that there is a phase delay and amplitude reduction in the blade loading due to the nonuniformities. These two effects depend on the reduced frequency of the propeller [54,55]. Since the BEM model is only used in the time-averaged sense, the change in blade loading as a function of the azimuth is not relevant, but the focus is put on the average change in performance due to the nonuniform inflow field. Furthermore, for the modeling of the slipstream-induced velocities, the average radial circulation distribution over the propeller disk is required rather than the detailed azimuthal variation [26].

B.   Slipstream Tube Modeling

The vorticity shed by the propeller blades in the helicoidal wake, together with the bound vorticity at the blades, will determine the induced velocities inside the propeller slipstream. Figure 5a presents a schematic representation of the helicoidal vortex sheet. Such a model is used for a frozen-wake LL or VLM to model the propeller performance. The induced velocities inside a point in the slipstream will depend on the relative position of the blades and hence the orientation of the vortex sheets. However, the overall time-averaged induced effects can be modeled by a much simpler model, representing the main features of a given propeller slipstream. Such a model is the STM [7,17,56]. In this model, the helicoidal vortex sheets are replaced by two continuous distributions of vorticity: the axial vorticity and the tangential vorticity, as indicated with the arrows (see Fig. 5b). Here, the tube at a single radial position is shown, but in reality, there is such a vortex tube at each radial segment. Together with the bound vorticity at the blades, the axial and tangential vorticity elements will determine the time-averaged slipstream velocities.

The STM allows for radial, azimuthal, and streamwise variations in vorticity throughout the streamtube. In the present paper, some simplifications are made to speed up the calculations. The shape of the slipstream tubes will be fixed, and hence the contraction of the slipstream is not taken into account. It is assumed that the slipstream axis remains parallel to the propeller axis [26]. Also, the slipstream roll-up will not be modeled, and hence the wake will not be force-free [57]. Nonetheless, the STM is a powerful and computationally inexpensive method to get a quantitative estimate of the induced velocities inside the slipstream. The induced velocity at point Q by an infinitesimal vortex filament of length dl with strength Γ is given by the Biot–Savart law:

$$d\boldsymbol{V}_Q = \frac{\Gamma}{4\pi} \frac{d\boldsymbol{l} \times \boldsymbol{r}_Q}{|\boldsymbol{r}_Q|^3} \quad (2)$$

where $d\boldsymbol{l}$ is the vector along the filament length, and $\boldsymbol{r}_Q$ is the position vector from the vortex filament to the control point Q. The contribution from the three separate vorticity components is shown for a single vortex filament in Fig. 6. Note that the vortex filaments are shown for a positive circulation gradient, which would occur close to the blade root. The calculation of the induced effect of the vorticity components is discussed separately in the following paragraphs.

1.   Tangential Vorticity Elements

The rings of distributed tangential vorticity are responsible for the axial-induced velocity in the slipstream. It is assumed that the
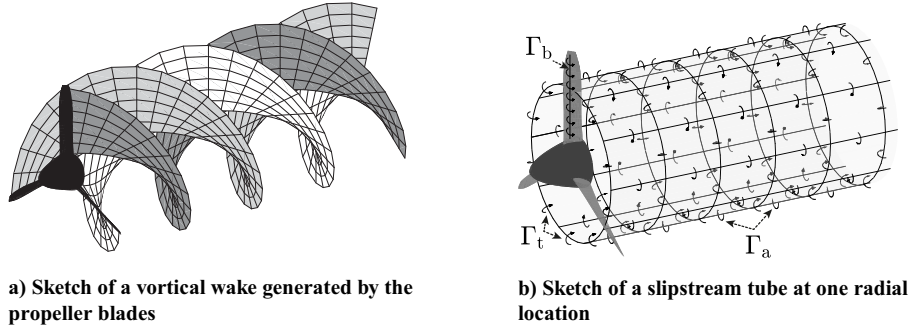
a) Sketch of a vortical wake generated by the propeller blades

b) Sketch of a slipstream tube at one radial location

Fig. 5   Schematic representation of a propeller slipstream (ignoring contraction).

a) Induced velocity due to the tangential vorticity elements

b) Induced velocity due to the axial vorticity elements

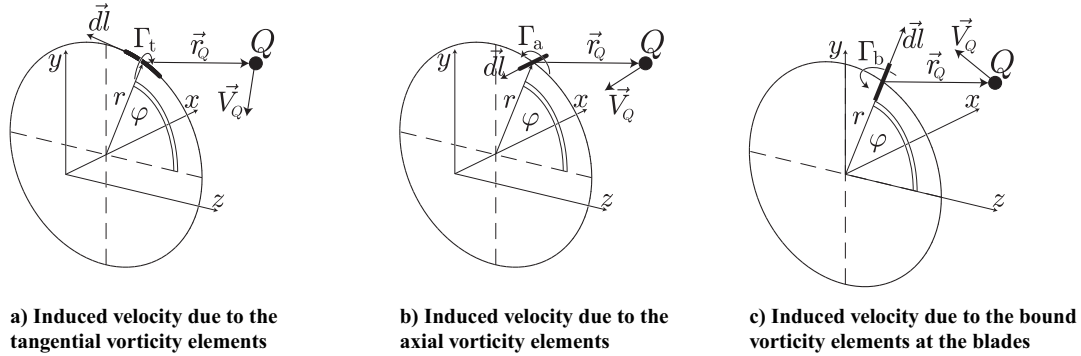**c) Induced velocity due to the bound vorticity elements at the blades**

Fig. 6   Induced velocity in point Q due to the three individual slipstream tube vortex filaments (derived from [7]).

slipstream does not deform, and therefore the radii of the tubes will remain constant for each streamwise position. To cover the whole slipstream, rings will be placed continuously in between the propeller disk ($x = 0$) and $x = \infty$, creating cylindrical surfaces for each radial segment, as shown in Fig. 5b. The strength of the distributed vorticity at a specific radial position (r) is determined by the change in the bound circulation of the propeller at this radial location ($d\Gamma_p$), which is being shed in the slipstream as free (trailing) vortices, directed in the tangential direction. The strength of the tangentially distributed vorticity (γ_t) of a single tube (fixed radial position) is a function of the local ratio between tangential velocity and axial velocity, which is a measure of the pitch angle of the helicoidal wake. So the higher the rotational speed given a freestream velocity, the more the shed vorticity is directed in the tangential direction. Note that the circulation distribution represents the azimuthal-averaged blade loading, including nonuniform inflow effects. The tangentially shed vorticity by the propeller blades is then averaged over the circumference of the ring ($2\pi r$) to get the time-averaged solution and is given by

$$\gamma_t(r) = \frac{V_t}{V_a} B \frac{d\Gamma_p}{2\pi r} \frac{dr}{dr} = \frac{\omega r(1-a')}{V_\infty(1+a)} B \frac{d\Gamma_p}{2\pi r} \frac{dr}{dr} = \frac{nB}{V_\infty} \frac{(1-a')}{(1+a)} \frac{d\Gamma_p}{dr} dr \tag{3}$$

where n is the rotational speed (rps), B the number of blades, V_a the axial velocity, and V_t the tangential velocity of the vorticity elements over the annulus considered. Note that in the original derivations by Veldhuis [7], the freestream velocity V_∞ and rotational speed ωr were used in the definition of the tangential vorticity strength, without the induction effects. However, it was found that this leads to an overestimation of the axial-induced velocity in the slipstream. Therefore, the axial induction (a) and tangential induction (a') factors are taken into account to make the tube model more accurate. Once the distributed tangential vorticity strength is defined, the induced velocity can be calculated using the Biot–Savart law. An infinitesimal tangential vortex filament on a ring with strength Γ_t will induce a velocity in point Q, as visualized in Fig. 6a. The strength of this tangential vortex filament can be calculated using the distributed tangential vorticity strength since it is equal to the total value of distributed vorticity over the small width of the filament (dx):

$$\Gamma_t(r) = \gamma_t dx = \frac{nB}{V_\infty} \frac{(1-a')}{(1+a)} \frac{d\Gamma_p}{dr} dr dx \tag{4}$$

Filling in this filament strength in the Biot–Savart law leads to a triple integral over all three dimensions to calculate the total induced velocity in point Q, caused by all the tangential vorticity elements. The formulation can be eased by using cylindrical coordinates for the vortex filaments (r, φ, and x). However, this triple integral cannot be solved analytically, meaning that the complete slipstream must be discretized so that the system can be solved numerically. Fortunately, due to the assumption of no contraction, the model can be simplified further since the integral can be solved analytically in the streamwise direction x. Therefore, the STM requires only discretization in the radial and azimuthal directions, reducing the computational cost compared to the full numerical discretization in the three dimensions. The three induced-velocity components in the x-, y-, and z-direction are calculated using the equations below, where φ is the angle of the vortex filament with respect to the positive z-axis (see also Fig. 6a). The tubes are discretized into N radial sections and M azimuthal sections. The full derivation of these equations can be found in Appendix A.

$$\begin{aligned} V_{Q,x} = \sum_{i=1}^{N} & \frac{nB}{4\pi V_\infty} \frac{(1-a_i')}{(1+a_i)} \left(\frac{\Delta\Gamma_p}{\Delta r}\right)_i r_i \\ & \times \sum_{j=1}^{M} \frac{c_{i,j}\cos(j\Delta\varphi) + b_{i,j}\sin(j\Delta\varphi)}{b_{i,j}^2 + c_{i,j}^2} \\ & \times \left(1 + \frac{x_Q}{\sqrt{x_Q^2 + b_{i,j}^2 + c_{i,j}^2}}\right)\Delta\varphi\Delta r \end{aligned} \tag{5}$$

$$V_{Q,y} = \sum_{i=1}^{N} \frac{nB}{4\pi V_\infty} \frac{(1-a_i')}{(1+a_i)} \left(\frac{\Delta\Gamma_p}{\Delta r}\right)_i r_i \sum_{j=1}^{M} \frac{\sin(j\Delta\varphi)}{\sqrt{x_Q^2 + b_{i,j}^2 + c_{i,j}^2}}\Delta\varphi\Delta r \tag{6}$$

$$V_{Q,z} = \sum_{i=1}^{N} \frac{nB}{4\pi V_\infty} \frac{(1-a_i')}{(1+a_i)} \left(\frac{\Delta\Gamma_\mathrm{p}}{\Delta r}\right)_i r_i \sum_{j=1}^{M} \frac{\cos(j\Delta\varphi)}{\sqrt{x_Q^2 + b_{i,j}^2 + c_{i,j}^2}} \Delta\varphi\Delta r \tag{7}$$

$$b_{i,j} = y_Q - r_i \sin(j\Delta\varphi) \quad c_{i,j} = z_Q - r_i \cos(j\Delta\varphi) \tag{8}$$

2. Axial Vorticity Elements

The axial vorticity elements are responsible for the swirl velocity in the slipstream. The distributed axial vorticity is placed on straight vortex lines, parallel to the axis of rotation and perpendicular to the tangential vorticity elements. So they form semi-infinite vortex lines in the streamwise direction for each given radial position at each azimuthal position. Lines will be placed over the whole circumference, again creating cylindrical surfaces (see Fig. 5b). Similarly to the tangential vorticity elements, infinitely many cylinders are placed along the radial direction. The strength of the axial distributed vorticity at a specific radial position is equal to the shed circulation in the wake in the streamwise direction, but spread out over the circumference of the cylinder:

$$\gamma_\mathrm{a}(r) = \frac{B}{2\pi r} \frac{d\Gamma_\mathrm{p}}{dr} dr \tag{9}$$

An infinitesimal axial vortex filament will induce a velocity in point Q, as visualized in Fig. 6b. The vector along the length of the axial vortex filament ($\boldsymbol{dl}$) is now directed in the x-direction. The strength of this axial vortex filament is equal to the distributed axial vorticity over the small width of the filament ($rd\varphi$):

$$\Gamma_\mathrm{a}(r) = \gamma_\mathrm{a} rd\varphi = \frac{B}{2\pi r} \frac{d\Gamma_\mathrm{p}}{dr} dr\, rd\varphi = \frac{B}{2\pi} \frac{d\Gamma_\mathrm{p}}{dr} dr d\varphi \tag{10}$$

Filling this filament strength into the Biot–Savart law leads to a triple integral similar to that of the tangential vorticity elements. Again, this integral can be solved analytically in the x-direction to remove the need for discretization in this direction and hence reduce the computational cost. The velocity components are calculated with the equations below:

$$V_{Q,x} = 0 \tag{11}$$

$$V_{Q,y} = \sum_{i=1}^{N} \frac{B}{8\pi^2} \left(\frac{\Delta\Gamma_\mathrm{p}}{\Delta r}\right)_i \sum_{j=1}^{M} \frac{c_{i,j}}{b_{i,j}^2 + c_{i,j}^2} \left(1 + \frac{x_Q}{\sqrt{x_Q^2 + b_{i,j}^2 + c_{i,j}^2}}\right) \Delta\varphi\Delta r \tag{12}$$

$$V_{Q,z} = \sum_{i=1}^{N} \frac{B}{8\pi^2} \left(\frac{\Delta\Gamma_\mathrm{p}}{\Delta r}\right)_i \sum_{j=1}^{M} \frac{-b_{i,j}}{b_{i,j}^2 + c_{i,j}^2} \left(1 + \frac{x_Q}{\sqrt{x_Q^2 + b_{i,j}^2 + c_{i,j}^2}}\right) \Delta\varphi\Delta r \tag{13}$$

3. Bound Vorticity Elements

Finally, the bound vorticity of the propeller also will alter the slipstream-induced velocities. The bound vorticity will be concentrated in annuli at the propeller disk. The influence of the bound vorticity will quickly drop as the streamwise position is increased, but this component is required in the calculations such that the swirl velocity is correct close to the propeller disk. The strength of the bound distributed vorticity at a specific radial position is simply that of the value of the bound circulation of all the blades combined, spread out over the circumference:

$$\gamma_\mathrm{b}(r) = \frac{B}{2\pi r} \Gamma_\mathrm{p} \tag{14}$$

An infinitesimal bound vortex filament located on the propeller disk will induce a velocity in point Q as visualized in Fig. 6c. The vector along the length of the axial vortex filament ($\boldsymbol{dl}$) is now directed in the radial direction. The strength of this bound vortex filament is equal to the distributed bound vorticity over the small width of the filament ($rd\varphi$):

$$\Gamma_\mathrm{b}(r) = \gamma_\mathrm{b} rd\varphi = \frac{B}{2\pi r} \Gamma_\mathrm{p} rd\varphi = \frac{B}{2\pi} \Gamma_\mathrm{p} d\varphi \tag{15}$$

The location of the vortex element is always at the propeller disk ($x = 0$), which means that there is no integral in the axial direction in the application of the Biot–Savart law. Therefore, the resulting equation can directly be converted to the numerical notation introduced before:

$$V_{Q,x} = \sum_{i=1}^{N} \frac{B}{8\pi^2} \Gamma_{\mathrm{p},i} \sum_{j=1}^{M} \frac{-y_Q \cos(j\Delta\varphi) + z_Q \sin(j\Delta\varphi)}{(x_Q^2 + b^2 + c^2)^{3/2}} \Delta\varphi\Delta r \tag{16}$$

$$V_{Q,y} = \sum_{i=1}^{N} \frac{B}{8\pi^2} \Gamma_{\mathrm{p},i} \sum_{j=1}^{M} \frac{x_Q \cos(j\Delta\varphi)}{(x_Q^2 + b^2 + c^2)^{3/2}} \Delta\varphi\Delta r \tag{17}$$

$$V_{Q,z} = \sum_{i=1}^{N} \frac{B}{8\pi^2} \Gamma_{\mathrm{p},i} \sum_{j=1}^{M} \frac{-x_Q \sin(j\Delta\varphi)}{(x_Q^2 + b^2 + c^2)^{3/2}} \Delta\varphi\Delta r \tag{18}$$

The induced velocity in point Q can be found by adding the individual contributions of the three separate vortex elements. When considering the discretization of the propeller slipstream in the radial and azimuthal directions, it is important that the mesh points of the vortex elements are not close to the evaluation point Q. Due to the inviscid nature of this vortex method, the induced velocities will become inaccurate if the evaluation point is in the vicinity of a vortex filament core due to the singularity there. Therefore, it is advised to take the evaluation points in between both radial and azimuthal control points. The implementation of a viscous-core model could reduce this discretization error.

C. Wing Modeling

The wing is modeled using a VLM with one panel in the chordwise direction, also known as a Weissinger VLM [58]. The benefit of using a Weissinger VLM compared to an LL is that the influence of the bound vortex segments is taken into account in the determination of the induced velocity of the complete wing vortex system. This is both needed to model swept wings and to include the 3D correction for the finite slipstream size. As discussed in Sec. II, there are corrections needed both in the 2D and 3D wing analysis of the wing aerodynamic performance to correct for the finite extent of the slipstream.

1. Two-Dimensional Airfoil Performance Including Jets

The importance of the jet height for the lift augmentation was first described by Ting and Liu [38] and later expanded by Prabhu [39]. In the potential flow approach, it is normally assumed that the pressure on both sides of the jet boundary must be equal. Furthermore, any slope of the dividing streamline induced by a disturbance, like the airfoil circulation, must be equal on both sides of the jet. For small jet heights, the circulation of the airfoil will induce a relatively large vertical and horizontal velocity component at the jet edge, meaning that the potential-flow boundary conditions are not met in a fixed-wake approach [37]. The problem of the finite jet height is analogous to a wing in an open jet wind tunnel or a wing in ground effect. The presence of close-by boundaries to the airfoil can be modeled by the application of the method of images. For the open-jet wind tunnel, the boundary condition requires satisfying the linearized constant pressure at both sides of the streamline [59]. The method used in wind tunnel wall corrections can be applied to a general case of an airfoil submerged in a jet surrounded by streams of different

velocities [38,39]. By the addition of the image vortices, the potential flow boundary conditions at the jet boundaries are satisfied. A schematic representation of the image vortex setup can be seen in Fig. 7a.

Here, a thin airfoil is located in a stream with velocity V_j. Above and below this middle region, there are two different domains with a different velocity, namely, V_∞. Note that the velocities of the upper and lower domains do not have to be equal to the freestream velocity or equal to each other. The thin airfoil is represented by a distributed vortex sheet placed at the chord line. The required circulation of the airfoil is found by requiring no normal velocity at the collocation points, including the effect of the images. The middle domain, including the airfoil, has height h and the upper region and the lower region are located at distance $h/2$ from the airfoil. The dividing streamlines between the different regions are used as reflection planes. As can be seen in Fig. 7a, the distributed vorticity of the thin airfoil is reflected at the upper dividing stream-line at an equal distance $h/2$ from that streamline. The strength of this image is not the same compared to the original circulation. The strength of the image as a fraction of the original circulation strength (ϵ) is a function of the velocity jump across the jet boundary (μ) [38]:

$$\mu = \frac{V_j}{V_\infty} \qquad \epsilon = \frac{V_j^2 - V_\infty^2}{V_j^2 + V_\infty^2} = \frac{\mu^2 - 1}{\mu^2 + 1} \qquad (19)$$

Note that this strength factor applies to the experienced induced velocity of the image in the jet domain. When the jet velocity would be less than the freestream velocity, the strength of the images is negative. Subsequently, the image vortices also have a reflection in the opposite dividing streamline. So at a distance of $\pm 2h$ from the airfoil, two other images are presented, both of integral strength $\epsilon^2\Gamma$. These images are also reflected again and again, and in this successive method, the influence of both the velocity increment as well as the slipstream height can be taken into account when finding the airfoil circulation. With the images present, an equivalent flow formulation of the jet domain can be defined. When considering the successive images that are located further away from the airfoil, the influence on the airfoil quickly becomes negligible due to the increase in distance and the decrease in strength, meaning that only a couple of image sets are needed to get a converged solution [60].

When solving the no-penetration condition at the airfoil control points, the addition of the images results in a reduction of the airfoil circulation strength ($\Gamma_j = \int \gamma(x)\,dx$) compared to the case with an infinite jet. The sectional lift l can then be calculated using the reduced circulation and the jet velocity ($l_j = \rho V_j \Gamma_j$). For infinitely small jet heights, the reduction in sectional circulation strength should be such that the resulting lift value is equal to that of an airfoil without any jet. The change in airfoil lift can be quantified using either the circulation ratio K_Γ or the sectional lift ratio K_l, comparing

the value of the airfoil in a jet to the freestream case. Thirdly, the lift coefficient ratio K_{C_l} is defined as the ratio of lift (or circulation) in a jet with finite height compared to that of an infinitely large jet. When considering the limiting cases for the jet height ($h \to 0$, $h \to \infty$), these three ratios (assuming $\mu > 1$) will theoretically range between

$$\frac{1}{\mu} \le K_\Gamma = \frac{\Gamma_j}{\Gamma_\infty} \le \mu \qquad 1 \le K_l = \frac{l_j}{l_\infty} = \mu K_\Gamma \le \mu^2$$

$$\frac{1}{\mu^2} \le K_{C_l} = \frac{l_j}{l_{j,\infty}} = \frac{\Gamma_j}{\Gamma_{j,\infty}} = \frac{K_\Gamma}{\mu} \le 1 \qquad (20)$$

For the case of a single jet, the strength of the images discussed above only applies for the equivalent flow in the middle domain. An equivalent flow can also be determined for the lower or upper domain, which will not be equal to that of the center domain, due to the velocity jump across the jet boundary. When, e.g., considering the lower stream, all the image vortices in this domain, as experienced by the middle stream, do not exist in the potential formulation of the lower domain itself. Furthermore, the influence of the airfoil circulation (in the middle domain) must be scaled with a factor $\sqrt{1 - \epsilon^2}$ to obtain the correct effective influence of the airfoil, as experienced in the lower stream. Equally, the effect of the successive images that are located in the upper stream, as experienced in the lower stream, also must be scaled. So the first image in the upper stream has an effective strength of $\epsilon\sqrt{1 - \epsilon^2}\,\Gamma$ as experienced by the lower stream.

The image method for an airfoil in a jet of finite height can be generalized to the case of an airfoil surrounded by numerous jets. When taking a large number of small streams, a continuous velocity profile can be approximated (see Fig. 7b). When using the same approach as for the airfoil in a single jet, the number of images quickly grows, since each initial image will be reflected in all the other dividing streamlines. Furthermore, successive images of different streams will now overlap, and hence the determination of the total strength of each combined image in every separate stream is nontrivial. When multiple streams are present, the scaling of all successive reflections across multiple velocity jumps is required to arrive at the correct combined image strength as experienced in the central stream, where the airfoil is located. When considering an airfoil surrounded by multiple streams (odd number), the equivalent flow in any of the considered streams can be described by an infinite series of equally spaced images. The strength of an (image) vortex located in stream j as experienced by the flow in stream i is denoted by $K(i, j)$ and can be calculated with the following recurrence relation [39]:

$$\beta_m K(m, m + s) = K(m - 1, m + s) - \alpha_m K(m - 1, m - 1 - s) \qquad (21)$$

where α_m and β_m are the strength factors of the images and are given by

a) Simplified axial velocity distribution assuming a single jet

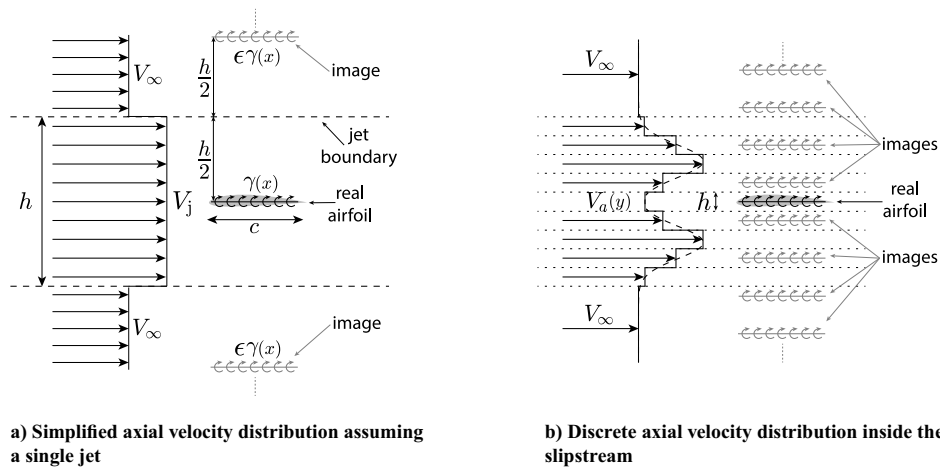b) Discrete axial velocity distribution inside the slipstream

Fig. 7 Image system for an airfoil in the middle of a jet and a smooth axial velocity profile.

$$\alpha_m = \frac{V_{m-1}^2 - V_m^2}{V_{m-1}^2 + V_m^2}$$

$$\beta_m = \sqrt{1 - \alpha_m^2} = \frac{V_{m-1}}{V_m}(1 - \alpha_m) = \frac{2V_{m-1}V_m}{V_{m-1}^2 + V_m^2} \qquad (22)$$

where V_m is the velocity in stream m. The middle stream, where the airfoil is positioned, is denoted with index 0. Assuming the total number of streams (M) to be odd, m and s vary between

$$-\frac{M-1}{2} + 1 \leq m \leq +\frac{M-1}{2} \qquad -\infty < s < +\infty \qquad (23)$$

Similar to the single-jet case, infinitely many successive images can be placed in the lowest and highest streams, which are unbounded, meaning the image index s can theoretically vary from minus to plus infinity. Note that airfoil circulation strength is included in the recurrence relation, so $K(0,0) = \Gamma$. For all other streams ($i \neq 0$), $K(i,i) = 0$, since an image vortex in a specific stream effectively does not exist in its own domain. Furthermore, all successive images that are positioned in the most upper and lower streams do not exist in their respective domains, so

$$K\left(-\frac{M-1}{2}, j \leq -\frac{M-1}{2}\right) = 0 \qquad K\left(\frac{M-1}{2}, j \geq \frac{M-1}{2}\right) = 0 \qquad (24)$$

For the example of a single jet, where the center stream is denoted with the index 0, the system of recurrence relations reduces to the above-mentioned values: $K(0, \pm j) = \epsilon^j \Gamma$ and $K(-1, j > 0) = K(+1, j < 0) = \epsilon^j \sqrt{1 - \epsilon^2} \Gamma$. For any arbitrary number of streams, the complete system of recurrence relations can be solved for the determination of all image strengths as experienced by the center stream, such that the effective circulation of the airfoil can be determined. Note that the thin airfoil approach taken in this study allows for infinitely thin streams. However, the same approach can be applied to thick airfoils, modeled with panel methods, since the effective flow in each stream can be calculated as functions of the complete system of vortex panels and associated images, also if the airfoil spans multiple smaller streams with different velocities.

For an airfoil submerged in a smooth velocity profile, so where the velocity jump across the different streams is small, a more elegant solution can be obtained, which reduces computational time. This can be achieved by decreasing the height of each stream, hence increasing the total number of streams. It turns out that for small velocity increments ($\Delta V_m = V_m - V_{m-1}$) across the stream boundaries, $\alpha_m \ll 1$ and therefore $\alpha_m \approx -\Delta V_m / V_m$, while $\beta_m \approx 1$. This means that the strength of the images experienced by the middle stream is simply related to the velocity jump across the different streams and that these images do not have to be scaled further for the determination of the equivalent flow in another stream, which leads to

$$m \geq 1 \rightarrow \quad K(0, 2m-1) = \alpha_m \Gamma = -\frac{V_m - V_{m-1}}{V_m} \Gamma$$

$$m \leq 0 \rightarrow \quad K(0, 2m-1) = -\alpha_m \Gamma = \frac{V_m - V_{m-1}}{V_m} \Gamma \qquad (25)$$

$$K(0, 2m) = 0$$

So every odd stream away from the middle stream contains an image. These images, located at a distance $\pm(2m-1)h$ from the airfoil, have a strength that is determined by the change in velocity, measured at the boundary at $\pm(2m-1)h/2$ away from the airfoil. This simplified image system is illustrated in Fig. 7b. Note that, with this simplified method, there are only as many images as streams in the velocity profile. However, the images located furthest away from the airfoil are located at twice the complete slipstream height, meaning that their influence in the middle stream is already very small, leading to a converged solution.

To the authors' best knowledge, no studies have applied the numerical correction technique by Prabhu [39] to properly model the effect of a nonuniform axial velocity profile on the airfoil lift in a propeller–wing case. In the current study, the circulation correction factor K_Γ for each wing segment that is inside the propeller slipstream is calculated using the method of images. The corrected 2D aerodynamic airfoil characteristics are then used in the 3D VLM modeling. Note that this method only focuses on the axial velocity component in the slipstream. In a 2D airfoil analysis, it is not possible to have a varying vertical velocity component in the flow domain since this would violate the mass continuity. So the effect of the varying vertical velocity profile for each wing segment, due to the 3D propeller-swirl field, cannot be modeled in each 2D analysis. Therefore, the vertical velocity at the collocation point is used to characterize the effect of the swirl velocity for each wing segment inside the slipstream.

2. Three-Dimensional Wing Performance Including Jets

When applying the 2D circulation correction for each section inside the slipstream, to account for the finite slipstream height and the nonuniform velocity profile in the calculation of the 3D wing aerodynamic performance, still an overestimation of the lift augmentation is obtained [60]. Therefore, only applying a 2D correction in the 3D VLM system is not sufficient. To satisfy the boundary conditions in the 3D potential flow analysis, a similar approach as in 2D has to be applied, so by adding image vortices. This was analytically done in the past by Rethorst [43], which led to complicated formulations due to the "odd" part of the image vortex system. Furthermore, this analytical approach was theoretically only applicable to a jet at the center of the wing, with a uniform axial velocity throughout this jet. The approach of Prabhu relieves these restrictions [39], and these generalizations were worked out for an LL formulation of the wing. In the current study, this generalization is applied to a Weissinger VLM approach.

Similar to the 2D analysis, the image method in 3D is introduced first with a single jet. Due to the circular slipstream boundary, the placement of the images is different from that for the 2D case. For the circular slipstream, the relation between the image position and the position of the vortex itself can be determined by using the jet center as a reference point. The images are placed at the inverse position compared to the distance from the real vortices to the center of the jet, as a fraction of the propeller radius. This means that a horseshoe vortex that is located inside the slipstream will have an image that is outside of the slipstream and vice versa. Due to this inverse relation, the image of vortex lines close to the slipstream edge on the inside is placed close to the edge on the outside and vice versa. However, the image of vortex lines close to the jet center is placed far away, possibly even past the wingtip. In the original formulation by Prabhu [39], only the trailing vortex lines of the system are considered since an LL approach was used, leading to an analytical expression for the jet effect. However, as shown by Rethorst [43], the influence of the bound portion of the horseshoe vortex needs to be included for a proper correction method.

Therefore, in the present study, the mentioned 3D image vortex approach is applied numerically to a set of horseshoe vortices using a VLM Weissinger approach. For the determination of the position of the horseshoe vortex images, the coordinates of the two edges of the bound vortex part are used. This means that the two edge points of the horseshoe vortex get flipped relatively to each other for the image, effectively resulting in an opposite circulation strength compared to the original one. Furthermore, this means that the width of the image is not equal to the original width of the horseshoe vortex. A schematic representation of this imaging process is shown in Fig. 8. For this 3D image approach, there is only one image for each horseshoe vortex. Depending on the collocation points' spanwise positions, both real horseshoe vortices and image horseshoe vortices induce velocities inside and outside the jet. Similarly, as for the 2D case, the strength of a horseshoe vortex located inside the jet must be scaled such that its influence is properly experienced outside of the jet and vice versa.

In the traditional VLM description, the influence of each horseshoe vortex on each collocation point at the 3/4 chord location is calculated. When considering the image vortex technique for the 2D modeling, the airfoil vortex elements are positioned in a single stream, while all the images are located in surrounding streams, where no other vortices are present. However, for the 3D modeling,
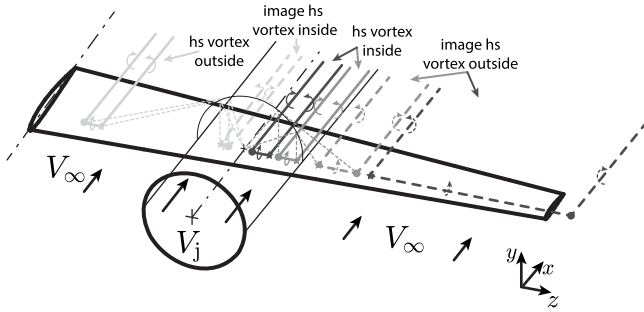
Fig. 8   Image vortex system of horseshoe vortices inside and outside a jet-like slipstream.

both the real vortices and the images are located inside and outside of the jet. So the equivalent flowfield due to the real and image horseshoe vortex system differs depending on the position of the collocation point (inside or outside the jet), which is illustrated in Fig. 9. When considering the domain inside the jet, the equivalent flow there is determined by three components, which are presented in the left equivalent flow column in Fig. 9. Firstly, there is the conventional induced velocity of all the horseshoe vortices that are inside the jet. Secondly, there is the influence of the images of these horseshoe vortices, which are all located outside of the jet. These images will have a strength of ϵ_1 compared to their original value. Thirdly, the velocity jump across the jet boundary scales the influence of the regular horseshoe vortices outside the jet, as experienced inside. So the strength of the horseshoe vortices outside of the jet is scaled by a factor of ϵ_2 to obtain their equivalent effect for the domain inside the jet. The strength of the images and the scaled horseshoe vortices is found similarly as for the 2D analysis:

$$\epsilon_1 = \frac{\mu^2 - 1}{\mu^2 + 1} \qquad \epsilon_2 = 1 - \frac{(\mu - 1)^2}{\mu^2 + 1} = \sqrt{1 - \epsilon_1^2} \qquad (26)$$

Note that the images of the horseshoe vortices outside of the jet, which are located inside the jet, do not contribute to the equivalent flow formulation inside the jet. The equivalent flow representations for both the domain inside and outside of the jet are shown schematically in Fig. 9. When considering the domain outside the jet, the equivalent flow is determined in a similar way as previously described. So next to the conventional induced velocity by all the horseshoe vortices outside of the jet, there is the additional influence of their images, located inside the jet, and the scaled influence of the horseshoe vortices located inside the jet, which is presented in the right equivalent flow column in Fig. 9.

When the jet velocity is higher than the freestream velocity ($\mu > 1$), ϵ_1 is positive. For the images of the horseshoe vortices inside the jet, denoted by the top-left equivalent flow illustration in Fig. 9, the strength is equal to $\epsilon_1 \Gamma$. Due to the relative inversion of the edge points of the image horseshoe vortex compared to the original horseshoe vortex, the strength is effectively flipped as well. So even though ϵ_1 is positive, the effect of the images experienced inside the

jet is that of a horseshoe vortex with a negative circulation. When the jet velocity is lower than the freestream velocity ($\mu < 1$), the strength of the images of the horseshoe vortices located inside the jet is negative ($\epsilon_1 < 0$), meaning that the effective strength experienced inside the jet is positive. For images of the horseshoe vortices that are located outside of the jet, denoted by the bottom right illustration in Fig. 9, the velocity ratio is inversed, meaning that their strength is equal to $-\epsilon_1 \Gamma$. When considering the scaling of the real horseshoe vortices to derive the equivalent flow in the different domains, the scaling factor is the same for both horseshoe vortices located inside and outside of the jet since ϵ_2 is always positive.

The discussion so far has focused on a jet with a uniform axial velocity profile in the radial direction. However, in a propeller slipstream, there is a nonuniform axial velocity in the radial direction. To model the effect of this velocity profile, a numerical approach similar to the 2D approach is taken: the slipstream is discretized in many different jets. However, in the 2D analysis, there are many small streams to model the continuous velocity profile. In the 3D analysis, the streams on both sides of the center line cannot be seen as separate streams. Rather, multiple jets of increasing radius are used to model the 3D axial velocity profile. This is schematically shown in Fig. 10, where two discrete jets are depicted.

In the example depicted in Fig. 10, jet 1 is the jet with the largest radius. Here, ϵ_1 and ϵ_2 can be determined using the respective jet velocity in this jet and the freestream velocity. For the second jet, which is smaller than the first one, the strength and scaling factors can be determined by using the velocity jump between the second jet and the first jet. This procedure can be repeated for a larger number of jets. The method of images (Fig. 9) can be applied for each discrete jet, leading to a whole system of images and scaled horseshoe vortices. When the number of discrete jets is increased and hence the velocity jump between the different jets is diminished, $\epsilon_1 \approx -\Delta V_m/V_m$ and $\epsilon_2 \approx 1$, as was the case for the 2D method. The total influence coefficient matrix, needed for the calculation of the VLM, is determined by the superposition of the individual jets. So the VLM system can be written as the conventional aerodynamic influence coefficient
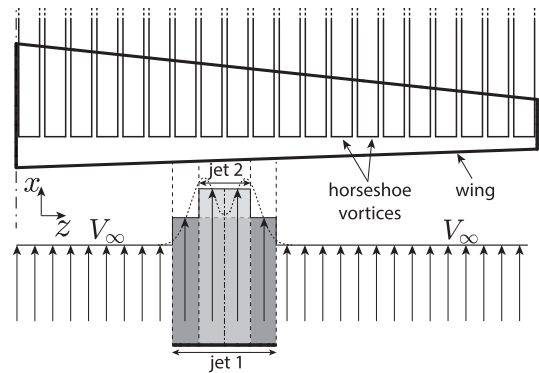

Fig. 10   Discrete representation of a continuous axial velocity profile in the spanwise direction.

Fig. 9   Equivalent experienced flow inside and outside the slipstream for horseshoe vortices inside and outside the slipstream.

matrix ([F]) plus the effect of the images and the scaling procedures ([G]) due to the velocity jumps between the different jets:

$$\left[\frac{[F]+[G]}{K_{C_l}(z)}\right]\Gamma_w(z) = -V_n(z) \qquad (27)$$

The system of equations can be solved for the unknown circulation strength of the horseshoe vortices (Γ_w) using the no-penetration condition in the collocation points. The induced velocities induced by the horseshoe vortex system must be equal and opposite to the normal component of the local velocity (V_n), which includes the slipstream-induced velocities at the collocation points. Note that for the determination of F and G, the effect of the local jet height for the wing segments inside the slipstream is not taken into account yet. So effectively, the 3D image method only accounts for the spanwise extent of the slipstream. For the conventional VLM approach without slipstream effects, the unknown circulation strength is solved without directly considering the 2D airfoil aerodynamic performance, leading to a thin airfoil (2π) lift-curve slope at each 2D wing segment. In the current method, when the G matrix is added, the found circulation strength of each wing spanwise segment is that of one with an infinite jet height. To include the 2D corrections for the nonuniform and finite slipstream height of the wing segments in the slipstream, the circulation strength of each horseshoe vortex must be corrected using the K_{C_l} correction factor. This factor can be simply implemented since there is only one chordwise panel in the used VLM approach. Since the circulation strength is unknown a priori, the two aerodynamic influence coefficient matrices (F and G) are divided by this correction factor to arrive at the correct circulation strength. Using the Biot–Savart law and the calculated circulation distribution of the wing, the induced velocity field at the propeller disk can be calculated and used as the next iteration input for the propeller BEM calculation.

The 3D image method is only a function of the (variation in) axial velocity V_a in the slipstream since the jet-like method does not account for the swirl velocity V_t. This also means that the effect of the swirl velocity, which is simply being modeled as an extra vertical velocity component experienced by the wing segments inside the slipstream, is not directly corrected. So the swirl velocity is being evaluated at the wing collocation points, and the component in the vertical direction alters the normal velocity component used for the no-penetration condition (V_n). This means that the effect of the nonuniformity in this vertical velocity component is not directly taken into account. Even if the swirl velocity were constant throughout the slipstream, the component of the swirl velocity directed in the normal direction would vary vertically for any 2D wing segment. To the authors' best knowledge, no suitable correction method exists that applies to the finiteness of the slipstream in terms of the swirl velocity. This means that the numerical method could lead to discrepancies compared to higher-order methods, like the higher-order free-wake approach.

3. Force Calculation

Once the circulation strength of all the horseshoe vortices is determined, the spanwise force distribution over the wing can be calculated. The force vector at each spanwise segment (F) can be found by applying the 3D vortex lifting law at a bound vortex line segment [61]. Therefore, the local velocity vector at the bound vortex line is needed, which includes the propeller-induced velocities. Note that the velocity vector at the bound control point will be different from that in the collocation point. The schematic representation of the force and velocity vector at the bound vortex segment is shown in Fig. 11.

Due to the induced velocities of the wing vortex system, the force vector will not be perpendicular to the freestream velocity. The downwash of all the horseshoe vortices at the bound vortex control point tilts the resultant force backward, resulting in the induced drag component. When adding the propeller-induced velocities, the induced drag can change direction [62]. This method of calculating the induced drag using the downwash at the bound vortex segments is different from the Trefftz plane technique, which often
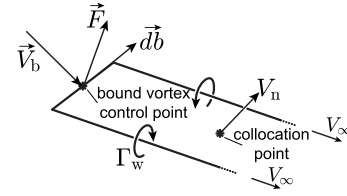

Fig. 11 Close-up of a single horseshoe vortex with the collocation and bound vortex control point.

is used in VLM models. For straight wings without sweep, the force calculation method at the bound vortex line for the induced drag works well since it produces an identical spanwise distribution as is obtained using the Trefftz plane technique.

However, for a swept wing, the induced-drag distribution becomes dependent on the chosen analysis position. For small to moderate sweep angles, the difference in lift distribution is very small between the bound vortex and the Trefftz plane approach. However, the spanwise distribution of the induced drag becomes completely different, even though the integrated value of the induced drag is not much affected. This same problem is described in the VLM solver AVL (Athena Vortex Lattice), where forces can both be defined parallel to the freestream or perpendicular to the quarter chord [63]. In the Trefftz plane analysis, the forces are merely defined as a function of the intensity of the chordwise loading in the streamwise direction. In the AVL manual, it is stated that the induced drag calculation is generally more reliable using the Trefftz plane analysis than the surface force integration using the vortex lifting law [63]. Therefore, a Trefftz plane analysis was implemented to find the spanwise distribution of induced drag for swept wings.

The propeller slipstream-induced velocities need to be added to calculate the correct induced drag d_i. The downwash generated by the wing vortex system and the images (v_w) in the Trefftz plane can be related to the equivalent downwash generated at the wing, since it is estimated to be twice as much in the Trefftz plane as on the wing in the case of a potential flow analysis. Since the propeller vortex system originates from a different axial position, it is difficult to relate the downwash generated by the propeller vortex system (v_p) in the Trefftz plane to that at the wing control points. Therefore, the downwash of the propeller system is calculated at the bound control points, and its effect on the induced drag is then added to the Trefftz plane analysis for the downwash of the wing vortex system:

$$d_i(z) = -\frac{\rho}{2}\underbrace{\Gamma_w(z)v_w}_{\text{@Trefftz plane}} - \underbrace{\rho\Gamma_w(z)v_p}_{\text{@wing bound vortex}} \qquad (28)$$

Due to the inviscid nature of the VLM, there are no viscous (drag) forces calculated. For small to moderate angles of attack, the viscous effects on the generated lift are small. However, not including viscosity means that there is no pressure and friction drag calculated in the VLM. If required, the viscous effects could be implemented in an empirical manner. The lift coefficient could be corrected by applying a correction to the effective angle of attack [64]. For the drag calculation, polars could be generated using, e.g., XFOIL to correlate the local C_l to the viscous C_d component, which can improve the modeling capabilities [35]. However, viscous-dominated flow phenomena such as high-lift conditions and slipstream–wing–flap interactions cannot be properly modeled with such empirical corrections. Note that such viscous correction is not taken into account in the current discussion, and therefore only the induced drag component of the wing is calculated. Unfortunately, validating the spanwise distribution of the induced drag component, using higher-order simulation or experimental data, has proven to be difficult since the spanwise pressure drag data include both the potential flow and viscous phenomena. Therefore, the induced drag component cannot be split from the viscous component [62]. The only way to use experimental or high-fidelity data is when comparing the integral induced drag component since this can be obtained using a far-field approach.

D. Computational Cost

The potential flow methods were chosen for their low computational cost. For the BEM analysis, either a direct analysis or an iterative approach could be chosen. For the direct analysis, the thrust is calculated based on the given input parameters and (nonuniform) inflow field. For the iterative analysis, the advance ratio and pitch setting are varied to maximize the propulsive or turbine efficiency for a given thrust condition as input. The complete code, which was generated using MATLAB® [65], was run on a standard workstation, having an Intel(R) Xeon(R) W-2223 processor with four cores. For the SIM simulation, where the mutual interaction is neglected and the propeller performance is directly calculated, the analysis takes a couple of seconds. For the FIM analysis of a single propeller–wing design, including the mutual propeller–wing interaction, the code takes in the order of a minute to run. This iterative procedure also includes the iterative BEM analysis of the propeller performance for a given T_C. Note that the code was not optimized for speed and was not run in parallel.

IV. Validation

The methods described in the previous section are validated against wind tunnel experimental data and higher-order numerical data in this section. For the validation of the BEM method and the STM, the experimental data were used [66,67], while high-fidelity numerical data were used for the validation of the VLM and propeller–wing system since no accurate experimental data were available in terms of a spanwise force distribution. The validation of the BEM model is discussed in Sec. IV.A, while the validation of the STM is discussed in Sec. IV.B. For both, a positive and a negative thrust condition were analyzed. Even though the negative thrust condition of the propeller is less representative of its design conditions, it was included to check the validity of the models away from the conventional operating conditions. Thereafter, the validation of the 2D and 3D VLM correction techniques is discussed in Sec. IV.C. Finally, the full chain of the models is validated for a propeller–wing system in Sec. IV.D.

A. Propeller Performance

1. Uniform Inflow

Firstly, the BEM is used to determine the integral performance of the propeller in terms of thrust and power for a given operational condition. The integral performance prediction also includes the azimuthal-averaged effects of the nonuniform inflow, caused by possible installation angles and wing-induced velocities. Subsequently, the most important parameter being modeled in the BEM is the circulation distribution over the blades since this is the input for the STM. The BEM method used in this study [49] has been validated by Goyal et al. [47]. In their study, the BEM was used to model the isolated propeller performance of a representative turboprop propeller, and the results were compared to experimental data of a wind tunnel test of the same propeller [66,67]. This experiment featured a three-bladed propeller, representative of a turboprop propeller [68]. The comparison between the experimental data and the BEM results was performed for a rather low blade pitch angle ($\beta_{0.7R} = 15°$) since the focus was put on analyzing both the positive and negative thrust regimes. Goyal et al. compared the integrated performance of the BEM method with that of the experiment in terms of C_T and C_P for a range of advance ratios [47]. Furthermore, the loading along the propeller blades was compared using the total pressure distribution.

The experiment was performed at $V_\infty = 30$ m/s, and therefore the chord-based Reynolds number at 70% of the blade radius was found to be around $2.35 \cdot 10^5$ and $1.34 \cdot 10^5$ for the positive and negative thrust cases, respectively [66,67]. In the positive thrust regime ($J = 0.60$), a good agreement between BEM and the experiment was found in terms of both integrated performance and blade loading. However, in the negative thrust regime ($J = 1.10$), there seems to be an underprediction in negative thrust by the BEM [47]. Furthermore, the negative power in this regime seems to be overpredicted by the

BEM method compared to the experiment, which was caused by the less accurate airfoil polar data for these unconventional operating conditions. At these negative thrust conditions, the RFOIL data seem to provide delayed stall predictions, leading to an overprediction in negative lift and an underprediction in drag [47].

Despite the extensive validation efforts in the study by Goyal et al. [47], no attention was given to the circulation distribution over the blades. Since the circulation distribution is directly used for the STM, an additional validation is presented here. The numerical results of the BEM are compared to the same experimental dataset used in the study by Goyal et al. [47]. Using the phase-locked time-averaged PIV data, the velocity field in the slipstream of the propeller was quantified for a given blade position [66]. These velocity field data are then used to estimate the circulation distribution on the blades in the wind tunnel. By using the Biot–Savart law, the circulation distribution on the blades that would result in the given velocity field could be found iteratively [69]. The circulation distribution derived from this estimation technique is compared to that from the BEM method for the case of $\beta_{0.7R} = 15°$, as shown in Fig. 12.

For the circulation distribution derived from the experimental velocity data, the uncertainty is added to the curves with the shaded regions. As can be seen, the circulation distribution for the propulsive condition ($J = 0.60$) obtained with the BEM method matches well with the experimental data. The integrated circulation value is underpredicted by 3.1% by the BEM compared to the experimental value, which is primarily caused by the differences at the blade root. Here, large deviations are present, which are caused by the inaccuracy of the polar data of these thick airfoil sections and also simplifying assumptions about the interaction between the blade root and hub/nacelle, which is estimated by Prandtl's hub correction [47].

The circulation distribution for the negative thrust condition ($J = 1.10$) derived from the BEM method shows larger discrepancies with the experimental data. The integrated circulation value is underpredicted by BEM by 11.4%. On the one hand, this is caused by the previously discussed discrepancies between the performance estimation between the BEM and the experimental data. On the other hand, the circulation estimation technique for the experimental data is less accurate for the negative thrust condition due to the observed flow separation on the propeller blade sections [47], and this effect is not taken into account in the mentioned estimation technique. For off-design propeller operations, like negative thrust conditions, the use of the circulation distribution derived from the BEM model could lead to discrepancies in the observed slipstream velocities between the STM and experimental data.

2. Nonuniform Inflow

In the current study, the nonuniform inflow conditions are taken into account in the calculation of the propeller performance. As discussed in Sec. III.A, this is done by discretizing the BEM also in the azimuthal direction, such that every location on the propeller disk can have different inflow conditions. To validate the capabilities
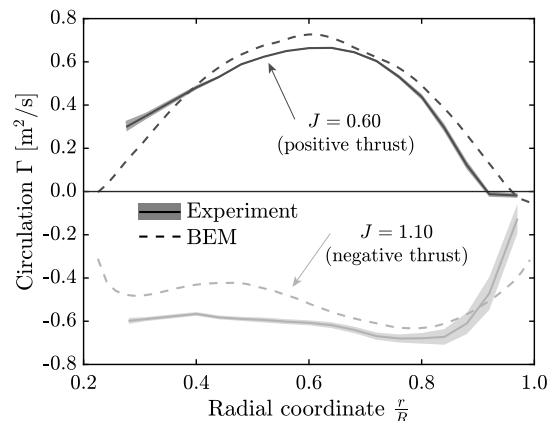

Fig. 12 Comparison of the propeller blade circulation distribution between BEM and experimental data for two different thrust settings.

of the BEM method to model a nonuniform inflow field, the integrated propeller performance of a propeller at a nonzero angle of attack is compared between BEM and experimental results. A propeller at an angle of attack is a specific instance of a nonuniform inflow field, where the effective rotational speed varies along the azimuth. In the experiment, the propeller angle of attack was varied while keeping the freestream velocity and advance ratio constant [67].

Figure 13 presents the change in both the thrust coefficient C_T and power coefficient C_P as a function of the propeller angle of attack (α_p) compared to the performance at $\alpha_p = 0°$, denoted with f_0. For the experimental data, a fourth-order polynomial was used to fit the raw data points. The 95% simultaneous confidence interval of these fits is included with the shaded region. Note that some of the fits (especially for C_P) featured a very small confidence interval, which makes it indistinguishable from the curve itself. In Fig. 13a and Fig. 13b, the results are shown for the positive thrust case and negative thrust case, respectively.

For both the positive and negative thrust conditions, the BEM results show reasonable agreement with the experimental data in terms of change in integral performance. When comparing the change in integral propeller performance calculated with the BEM for the positive thrust ($J = 0.60$), the increase in thrust is slightly underestimated compared to the experimental trend. At a propeller angle of 20°, where the increase in thrust is around 25–30%, the prediction by BEM is 1.5% lower than in the experiment. At the same time, the increase in power is overestimated compared to the observed experimental data. At $\alpha_p = 20°$, where the increase in power is around 10–15%, the increase in power by BEM is 2.0% more than in the experiment. Due to the mentioned differences in thrust and power, the BEM results will show a larger deviation in terms of the increase in propeller efficiency. This increase will be underestimated by the BEM method compared to the experiment. These discrepancies could lead to an underprediction in axial velocity in the slipstream-induced velocities, while the swirl might be overestimated at high propeller angles of attack using the BEM compared to the experimental results.

For the negative thrust case ($J = 1.10$), the BEM method also seems to predict the observed trends in the experiment reasonably well. The reduction of negative thrust with increasing angle of attack is overestimated by the BEM method, where the decrease in thrust is 0.8% more at $\alpha_p = 20°$ compared to the experimental value, at which the reduction in negative thrust is about 20%. The reduction in the negative power is underestimated in the BEM compared to the experiential data. The decrease in power is around 2.0% less at $\alpha_p = 20°$ than in the experimental data, at which absolute reduction in negative power is about 25%. This means that the reduction in turbine efficiency, the relevant efficiency in this regime [66], is underestimated by the numerical method. So the BEM method seems to capture the effects of a propeller angle of attack on the integrated performance rather well.

However, due to the simplistic implementation, the blade loading and its azimuthal variation might not be accurate compared to the experimental data.

B. Slipstream Velocities

The original formulation of the STM model was originally derived by Veldhuis [7]. However, it was never validated with experimental data. In this study, the STM is coupled with the BEM model to calculate the slipstream-induced velocities for a given propeller performance. Radial distributions of axial and tangential velocity at multiple axial positions behind the propeller blades were extracted from the PIV data mentioned before [66]. These velocity distributions are compared to the results from the STM for both the positive and negative thrust settings, using the circulation distributions (Γ_{BEM}), as shown in Fig. 12. The results are shown in Fig. 14a and Fig. 14b for the axial and tangential velocity, respectively. These radial distributions were obtained at $x/R = 1.00$ behind the propeller disk.

Note that a convergence study regarding the azimuthal and radial discretization was performed but is left out of this paper for clarity. The required resolution of the radial and azimuthal discretization of the STM was derived based on a convergence study. The resolution of the radial discretization is primarily driving the resolution of the gradient of the circulation and, with that, the overall accuracy of the velocity distribution. The resolution of the azimuthal discretization is more determining the accuracy related to the positioning of the control points with respect to the vortex filaments. For the selected resolution of 25 radial points and 40 azimuthal points, the error was less than 0.1% compared to the equivalent infinitely fine mesh. When the discretization in the streamwise direction is included, hence the analytical integration in x is not performed, the STM solution was only improved marginally compared to the fixed radius approach. However, the computational cost was approximately increased by a factor of 100. In the current study, it was therefore chosen to focus on the results based on the fixed radius approach, since this approach seems more suitable for propeller–wing interaction studies due to the low computational cost.

Overall, the trends are captured well with the STM, considering its low computational cost. For the radial distribution of axial velocity, the STM overpredicts the axial induction in the positive thrust case ($J = 0.60$). At the peak values at around $0.6R$, there is about a 15% overestimation of the axial induction in the STM values compared to the experimental values. This could partially be caused by the small overestimation in circulation distribution by the BEM model compared to the experimental data. Close to the tip of the propeller, the STM starts to deviate more from the experimental data. This is partially because the contraction of the slipstream is not taken into account in the STM. Furthermore, the loading at the tip at this specific advance ratio turned out to be negative, and higher-order modeling techniques also have difficulties modeling the reduction in axial velocity here [47].
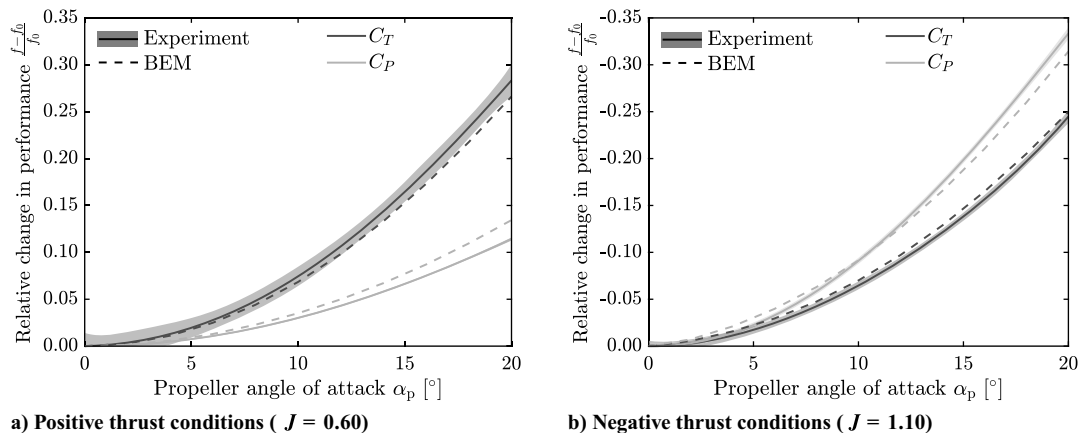

a) Positive thrust conditions ($J = 0.60$)

b) Negative thrust conditions ($J = 1.10$)

Fig. 13 **Comparison of the change in propeller performance for different propeller angles of attack between the BEM and experimental data for two different thrust settings.**

a) Axial velocity distribution
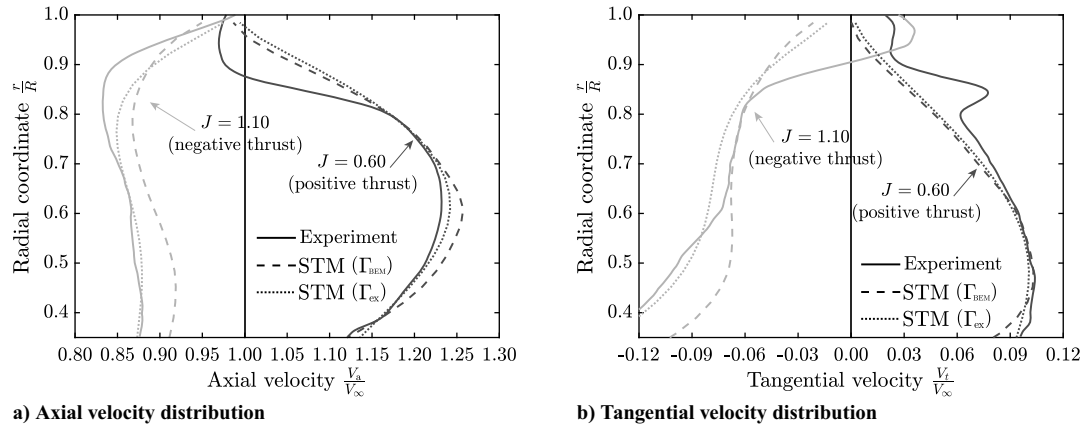
b) Tangential velocity distribution

Fig. 14 Comparison of the radial distributions of axial and tangential velocity at $x/R = 1.00$ between STM solutions and experimental data for two different thrust settings.

For the negative thrust condition ($J = 1.10$), the axial velocity calculated with the STM shows more deviations from the experimental data than for the positive thrust setting since differences in the axial induction of around 40% are observed at around $0.85R$. However, the general trends are similar between the STM and the experiment, but with an offset over the complete blade span. As for the positive thrust case, the difference in the used circulation distribution could cause the underestimation in the axial velocity reduction of the STM. The difference in circulation distribution between the BEM and the experimental data is much larger for the negative thrust setting than for the positive thrust setting. Furthermore, the negative thrust setting has been shown to exhibit much more separated flow over the blade sections, especially at the region where the largest discrepancies are observed between the STM and the experiment [47,67]. Therefore, it is expected that more viscous effects are present that reduce the axial velocity distribution further.

To eliminate the error in the input data used for the STM, the estimated experimental values for the circulation distribution (Γ_{ex}) are used as input for the STM. The resulting radial distribution of axial velocity at $x/R = 1.00$ based on this experimental circulation distribution is also presented in Fig. 14a. It can be confirmed that part of the discrepancy originates from the existing differences in the circulation distribution between BEM and the experiment since the use of the experimental circulation distribution reduces the discrepancies. Especially for the negative thrust condition, the math between the STM and the experimental axial velocity distribution is greatly improved. At the tip, discrepancies still remain, which also could originate from the assumption of no contraction in the STM. Note that the estimation technique [69] to get the experimental circulation distribution is also limited to potential flow assumptions and therefore might not be fully correct, contributing to the remaining discrepancies.

For the radial distributions of tangential velocity (see Fig. 14b), the STM shows a reasonable match with the experimental data. Especially for the positive thrust setting, the STM shows a good agreement for the inboard part of the slipstream. Closer to the tip, there is more deviation, similar to the radial distribution of axial velocity. Note that, in the STM, there is no change in the tangential velocity away from the propeller blades due to the potential flow assumptions. The experimental tangential velocity distribution shows a sudden peak at around 85% of the blade radius. It was hypothesized that this effect originated from the tip vortex in combination with the negative loading at the tip at the used advance ratio [66]. For the negative thrust condition, the overall trend in tangential velocity is captured, and at around 75% of the blade radius, there is almost no discrepancy with the experimental data. However, close to the tip and the root, there is a large offset of the STM compared to the experimental data due to the difference in circulation distribution observed between the BEM and the experiment and due to the viscous effects that occur more in these regions.

When considering the radial distributions of tangential velocity, the use of the experimental circulation distribution in the STM leads

to a small improvement in the match with the experimental data. For the positive thrust setting, there is a small shift in tangential velocity, and close to the root, the values remain close to that of the experimental data. For the negative thrust setting, the match between the STM and experimental data is improved greatly. Especially at the inboard part of the blade, the discrepancies between the STM and experimental data are much reduced compared to the STM solution derived with the BEM circulation distribution. However, at around 75% of the blade radius, there is slightly more discrepancy with the experimental data compared to the STM solution derived with the BEM circulation distribution.

To conclude this section, the STM seems to be able to capture the general trends of the axial and tangential velocity distribution well for (conventional) positive thrust conditions. There is an overestimation in the axial velocity of the STM compared to experimental data, but given the low computational cost, it seems like an attractive method to calculate slipstream velocities for the propeller–wing interaction modeling. For more unconventional propeller operations, like negative thrust, the BEM results showed larger deviations from the experimental data due to the separated flow around the blade segments in this condition [47]. This incorrect modeling of the BEM is then propagated into the calculation of the circulation distribution on the propeller blades, which in turn means that there is a larger deviation in the calculated slipstream velocity distributions for the negative thrust setting compared to the experimental data.

C. Wing Performance

In this section, the validation is presented of the numerical tools that are used to model the aerodynamic performance of an airfoil and complete wing that are submerged in a slipstream. Since the image vortex technique in both the 2D and 3D analyses is only based on the axial velocity component, no swirl velocity is taken into account in the validation. Furthermore, to simplify the validation, a jet-like slipstream is modeled, meaning a constant axial velocity. In Sec. IV.C.1, the 2D airfoil analysis is discussed, after which the 3D wing analysis is presented in Sec. IV.C.2.

1. Two-Dimensional Airfoil Performance in a Jet

The numerical method described in Sec. III.C.1 is validated with the use of higher-order numerical data for the case of an airfoil submerged in a jet. This is done by modeling a NACA 0012 airfoil submerged in a jet of different heights for two different velocity ratios. The validation data were obtained with the use of both 2D RANS [60] and MSES simulations [70]. The 2D numerical model with the image vortex technique does not include any viscous effects. Therefore, RANS simulations were performed in a potential flow manner by solving the Euler equations to avoid any viscous effects. It turned out that numerical diffusion was influential to the results, requiring a very fine mesh in the RANS simulations, especially to avoid diffusion of the slipstream edges [60]. In the RANS simulations, the jet inlet was defined on the inlet plane, far away from the

airfoil. The MSES simulations benefit from the fact that the solutions are derived from a potential flow initialization [71]. Furthermore, an actuator disk can be defined somewhere in the domain after which the inlet conditions are solved iteratively to find the correct flowfield [70,72]. Also in the MSES simulations, viscous effects were not included to match with the low-order numerical model.

The validation of the numerical results of the 2D image technique is shown in Fig. 15. The NACA 0012 with chord c is evaluated at $\alpha = 2°$ in a jet of height h. The lift ratio K_l is calculated for different slipstream heights. The data points are shown for the cases of $V_j = 1.5V_\infty$ and $V_j = 2.0V_\infty$. For an infinitely high slipstream, the lift ratio would be equal to the velocity ratio squared, which is indicated by the dashed line. As can be seen, the lift augmentation of the airfoil is almost not influenced by the slipstream height from $h/c = 6$ onward. For smaller values of h/c, the lift is lower than would be estimated from an infinite slipstream height. Especially for $h/c < 1$, the lift drops quickly with reducing height. The numerical results show a good agreement with both the CFD and MSES analysis results. In particular, the MSES results, which do not suffer from artificial diffusion like the RANS results, show a good match with the numerical data. The RANS data deviate from the MSES results for small jet heights, due to the difficulty in defining the exact slipstream height at the airfoil, given a certain inflow field [60]. In the MSES simulations, the position of the jet can be more precise since the actuator disk was defined closer to the airfoil.

The discrepancies between the numerical results and the MSES results are larger at small h/c values, which is the domain where the lift ratio is heavily influenced by the slipstream height. Defining the slipstream height at these small jet heights becomes difficult, even for the MSES simulations, since the slipstream will flow around the top and bottom of the airfoil, effectively increasing the height [70]. Furthermore, the small perturbation theory used in the numerical model is no longer valid when the slipstream edges come very close to the airfoil. Nonetheless, the method of images seems to be a powerful and computationally cheap way to correct the 2D airfoil lift for the finite slipstream height.

2. Three-Dimensional Wing Performance with a Jet

For the 3D implementation of the image vortex technique, again a jet-like slipstream, without swirl, is modeled, and the numerical wing performance is compared to that of a CFD simulation [60]. In Fig. 16, the results of the analysis are shown. A straight, untwisted wing is modeled with an aspect ratio of 10 and no taper. For this wing, the C_l distribution along the span is shown with the clean wing lift distribution as a reference. The jet is added at the center of the wing, with $D_p/c = 2$, meaning that there is a maximum h/c of 2 at the center, and this value decreases toward the sides. The jet velocity was set to 1.5 times the freestream velocity. Two RANS simulations were performed: one with the circular jet as described and one with a
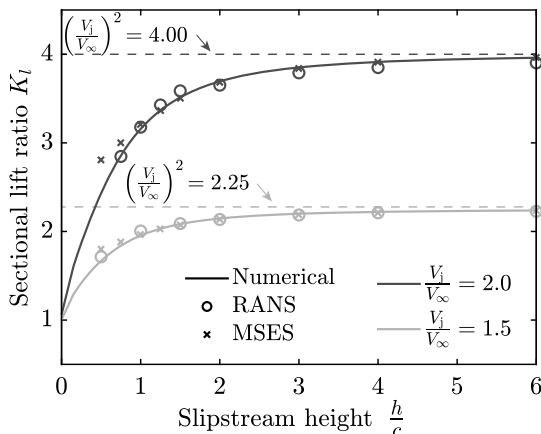

Fig. 15 Comparison of the lift ratio at different slipstream heights for two different jet velocities between the numerical data and the higher-fidelity analyses.
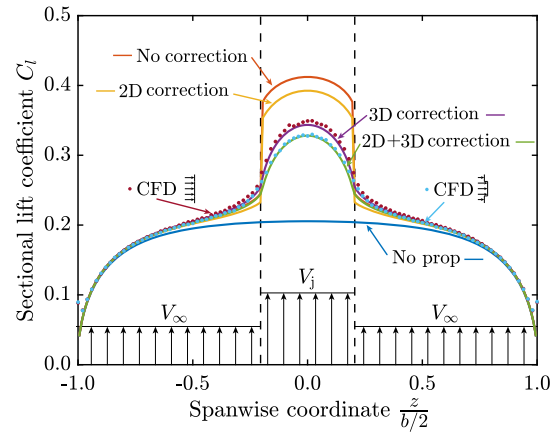

Fig. 16 Comparison of the spanwise lift distribution of a wing with a jet at the center between the numerical data and CFD results.

rectangular jet that has the same width as the circular jet but with a very large height. This is done to test the implementation of the 2D corrections within the 3D correction approach.

As shown in Fig. 16, the lift distribution is greatly overestimated in the slipstream region when no corrections are applied. The increase in lift at the wing segments inside the slipstream is at least 66% higher than observed in the CFD data, which leads to an overestimation in integral C_L of 8.2%. This would be the result of the conventional way of calculating the slipstream-induced change in wing performance by simply adding the induced velocities to the VLM horseshoe vortex system. When the 2D image vortex technique is applied to alter the 2D wing segment circulation strength, the lift augmentation is reduced compared to the no-correction case. However, only applying the height correction at the wing segments submerged in the slipstream is not sufficient to achieve a realistic lift distribution as shown by the RANS results. Locally, there is still an overestimation in the lift augmentation of at least 50% for wing segments inside the slipstream, compared to the RANS data, leading to an integral C_L that is 5.2% higher.

When the 3D image technique is applied, the spanwise extent of the jet is effectively taken into account in the VLM, and the result shows that the lift augmentation is further reduced compared to the 2D correction case. For this analysis, only the 3D images are considered, so neglecting the 2D height corrections for the spanwise segments submerged in the jet. This is equivalent to the CFD case with the rectangular jet. As can be seen, the comparison of the VLM data with the CFD data shows a good match between the two. There is a small underprediction by the VLM, but the integrated C_L differs by only 1.5%. When both the image vortex techniques are applied, the calculation of the spanwise circulation strength is also corrected for the local jet height of the spanwise segments submerged in the circular jet. This leads to a further reduction in the lift augmentation, matching with the CFD data for the case of a round jet. Again, there is a small underprediction by the VLM compared to the CFD data, but the difference in the integrated C_L is also around 1.2%. So it can be concluded that implementing both the 2D and 3D image corrections leads to a much better estimation of the wing lift distribution for a wing with a jet. Similar to the 2D results, the jet-like simplification does not include any swirl velocity. In the next section, the validation of a realistic propeller–wing system is discussed, where the swirl effect is added.

D. Propeller–Wing Performance

1. Propeller–Wing Model

In the previous subsections, the individual submodels are validated. As a final validation step, a full propeller–wing setup is modeled, hence having a realistic nonuniform axial velocity profile in the slipstream and also including the swirl velocity component. The used geometry is that of an experimental setup, tested in the LST wind tunnel at DNW, which was part of the FutPrInt50 project [73]. Here, a
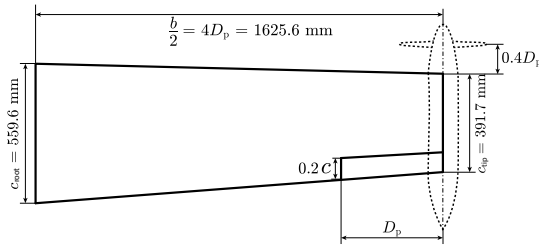
Fig. 17   Experimental setup with a tip-mounted propeller.

tapered wing was designed with a nonswept quarter-chord line and a taper ratio λ of 0.7. The propeller was installed at the tip to investigate the potential benefits of a tip-mounted propeller. Furthermore, the wing contained an aileron close to the tip. The planform of the setup can be seen in Fig. 17. The TUD-XPROP was used for the setup, this time as the six-bladed configuration instead of the three-bladed one used in the isolated propeller experiments [66]. The tip of the wing without the propeller was defined to be at the center line of the propeller–nacelle setup.

When the nacelle is installed, the spanwise lift distribution is altered compared to the clean-wing configuration. During the experiment, it is not possible to isolate the nacelle effects from the propeller effects. Therefore, the same experimental setup was analyzed using RANS CFD simulations, in which the propeller was modeled using an actuator disk. Using this approach, the nacelle could be removed while keeping the actuator disk in the same position compared to the propeller disk. This configuration is most similar to the VLM numerical model, in which also no nacelle effects are included. The input on the actuator disk was defined by high-fidelity numerical (LBM) simulation results of the installed propeller [74]. The corresponding T_C of the actuator disk was found to be 0.045, which is a rather low thrust setting, representative of cruise conditions. Note that the aileron was not modeled in the CFD simulation or VLM simulation. The wing was modeled to be at an angle of attack of 0°, while the propeller disk was tilted down by 3.5°.

2.   RANS Setup

The RANS equations for compressible flow were solved using ANSYS® Fluent 2019 R3 [75], which is a commercial, unstructured, finite-volume, cell-centered solver. The propeller was modeled using the actuator disk approach [76], allowing for steady-state simulations. As shown in Fig. 18, the computational domain encompassed half the wingspan and was semispherical with a radius of 100 times the mean aerodynamic chord of the wing ($\bar{c}$). This domain size was selected based on previous studies of similar configurations [77–80]. The block of the domain in the vicinity of the wing, which contained the finest mesh, extended $1\bar{c}$ upstream and $5\bar{c}$ downstream of the leading edge of the wing root. The actuator disk was positioned within the cylindrical region upstream of the wing, while the downstream cylindrical region was defined to capture the strong gradients

in flow properties within the propeller slipstream. The semispherical boundaries were treated as pressure far-field and symmetry planes, with the wing modeled as a no-slip wall. Air density was computed using the ideal gas law, and dynamic viscosity was determined via Sutherland's law. The turbulence modeling was based on the Spalart–Allmaras method, incorporating modifications proposed by Dacles-Mariani et al. [81,82].

Grid generation was performed using ANSYS Meshing. Adjacent to the no-slip wall region, a triangular wall grid with layers of semistructured prismatic and tetrahedral elements was applied at the wing. A structured grid was used within the cylindrical regions to minimize the diffusion of the propeller slipstream, while an unstructured hexagonal grid was created in the far slipstream and upstream of the propeller to reduce the total element count. The first layer thickness of the inflation layers was adjusted to maintain $y^+ \leq 1$ as required by the Spalart–Allmaras turbulence model. Grid density in the whole domain was controlled by wall refinement of no-slip walls and volume refinement. The grid density was highest in the vicinity of the wing and propeller, gradually decreasing in the far field to optimize computational cost. To ensure the reliability and accuracy of the simulations, a systematic grid dependence study was conducted, details of which are provided in Appendix B.

3.   Results

Firstly, the results of the clean wing are discussed in terms of the spanwise lift distribution. Since the VLM does not model any effects of the airfoil camber and the thickness, the effective angle of attack of the wing was varied until the integrated lift coefficient C_L of the VLM was the same as that of the RANS CFD simulation. Therefore, the effective angle of attack in the numerical model was set to 3°, while the RANS simulation was performed for $\alpha = 0°$. Changing the angle of attack in the model simply shifts the lift curve to match with the RANS results. The comparison between the VLM and the CFD results can be seen in Fig. 19a. The clean wing lift distribution shows a good match between the two methods. For the CFD simulation, there is slightly more lift generated at the inboard part, which is probably caused by the influence of the proximity of the walls of the domain. At the same time, there is slightly less lift at the tip region. This is caused by the wingtip of the model. The VLM models the wing with a straight and cutoff wingtip, while the model used in the RANS simulations featured a rounded wingtip, where the chord quickly reduces to zero.

For the case with the propeller, the results from the VLM and CFD are shown in Fig. 19b. The results from this VLM simulation include the effects of the nonuniform axial velocity profile in the slipstream and the swirl velocity. Note that both the spanwise distributions of lift are shown for the VLM results with and without the correction techniques. Due to the low thrust setting, the lift augmentation is limited. Since the propeller was rotating inboard-up, there is an increase in lift both due to the axial and swirl velocity. The VLM seems to overpredict the increase in sectional lift due to the propeller slipstream velocities compared to the CFD data.
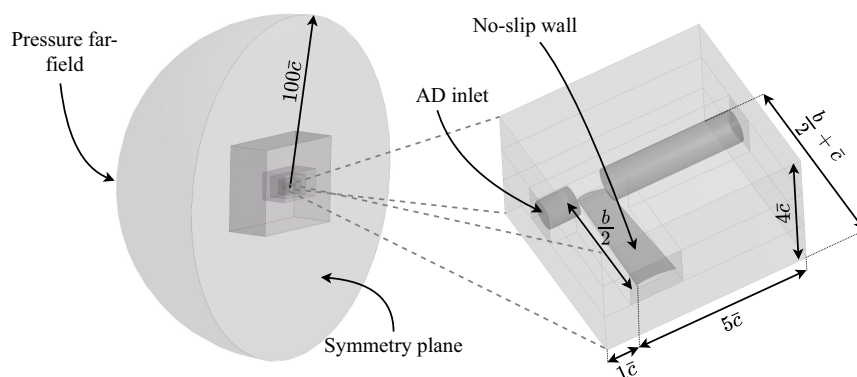

Fig. 18   Numerical domain and boundary conditions for the RANS simulations.

a) Clean-wing configuration   b) Installed propeller-wing configuration
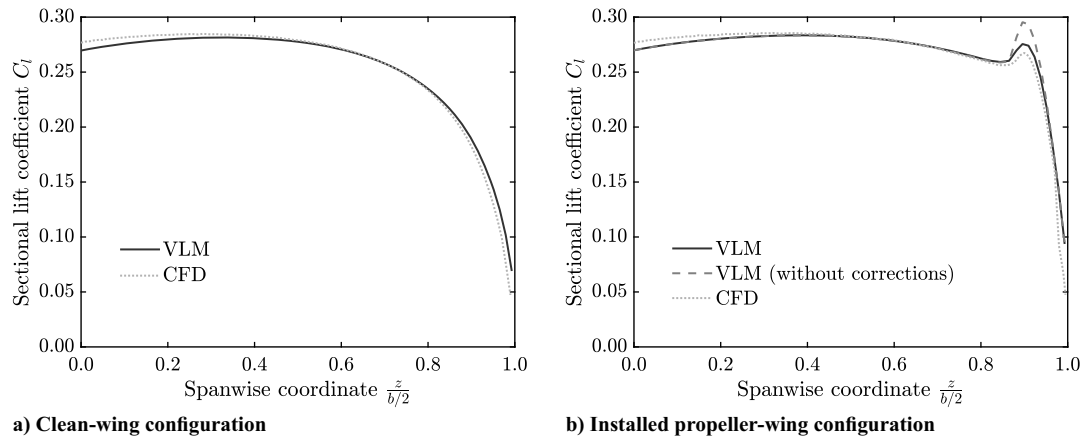
Fig. 19   Comparison of the sectional lift distributions for the clean-wing and the propeller–wing system between the VLM and CFD results.
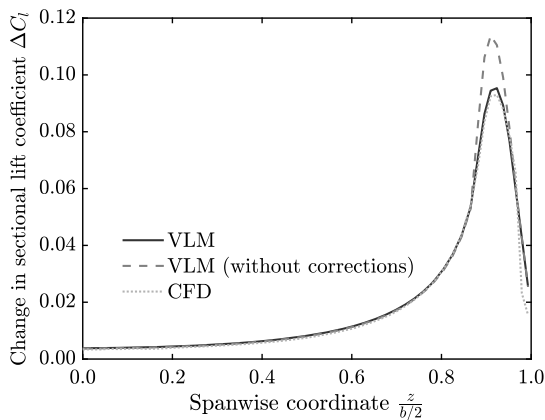

Fig. 20   Comparison of the change in sectional lift distribution for the propeller–wing system between the VLM and CFD results.

However, the lift at the tip was already higher in the VLM for the clean wing. In Fig. 20, the change in sectional lift is shown for the VLM and RANS simulation. As can be seen, the lift augmentation seems to be almost identical between the RANS and VLM results when the 2D and 3D corrections are included.

The difference in integrated C_L between the RANS and VLM results is only about 0.1%. As discussed before, the STM overpredicts the axial induction slightly, possibly leading to a marginal overprediction in lift augmentation. Furthermore, the addition of the swirl to the VLM without any correction could lead to an overprediction of this swirl effect. As can be seen, neglecting the correction methods increases the lift augmentation significantly, increasing the overprediction in lift to 1.7% compared to the CFD data. Locally, inside the slipstream region, the increase in sectional lift values is overestimated by up to 25% when not including the corrections. This highlights the need for the 2D and 3D correction techniques in the modeling of the propeller–wing systems. This becomes even more relevant when the T_C is increased for the propeller because that leads to increased slipstream-induced velocities and thus larger perturbations of the wing lift distribution.

For the validation of the complete propeller–wing system, only the spanwise lift distribution is compared between the RANS and the VLM results. As mentioned before in Sec. III.C.3, the spanwise drag distribution from the RANS simulation also contains pressure drag components that are originating from viscous effects. Furthermore, it is not possible to extract the inviscid drag component from the total spanwise drag force in the RANS simulation. Therefore, comparing the induced drag distribution from the VLM directly with the drag distribution from the RANS simulations will yield incorrect conclusions.

V.   Conclusions

Multiple low-order potential flow-based methods are derived and combined such that the interaction effects can be modeled accurately and quickly. Considering the low computational cost, the BEM method is an attractive way to model propeller performance. Furthermore, the added azimuthal discretization of the propeller disk allows for the modeling of nonuniform inflow fields. This means that both the effect of a propeller installation angle and the upstream influence of the wing on the propeller performance can be included. From the BEM method, the circulation distribution over the blade is calculated, which is used in the STM. The STM is a time-averaged and fixed-wake vorticity model to calculate the propeller-induced velocities inside the slipstream. The cost of the STM is kept low by assuming no contraction of the slipstream, which allows for analytical integration in the axial direction. A standard VLM implementation was used to model the wing performance. However, instead of simply adding the propeller-induced velocities to the horseshoe vortex system, image vortex techniques are implemented in both the 2D and 3D senses to account for the finite dimension of the slipstream, which reduces the lift augmentation compared to conventional VLM approaches.

The BEM method used to model the propeller performance was validated using experimental data. For the positive thrust case, the circulation distribution is modeled accurately with the BEM method since only a 3.1% underprediction was found in the integral circulation value compared to experimental data. For the negative thrust setting, where the aerodynamics of the propeller are more dominated by viscous effects, such as flow separation, the circulation distribution is less accurate, where an 11.4% underestimation was found between BEM and the experimental results. The accuracy of the BEM polar data and, with that, the accuracy of the circulation distribution have also a large influence on the STM accuracy. The ability to include a nonuniform inflow field in the BEM was validated for the case of a propeller at an angle of attack. The change in integral performance was compared, and the BEM shows good agreement with experimental data in terms of the change in thrust and power coefficient for a propeller at an angle of attack.

The STM model was validated using experimental PIV data, where radial distributions of axial and tangential velocity were obtained at different streamwise positions. For the positive thrust case, the match between the STM and the experimental slipstream velocities is good, considering the low computational cost. For the negative thrust conditions, there was a larger offset noted in the axial velocity between the STM and the experimental data than for the positive thrust condition. Most of the difference in the axial induction between the STM and the experimental data is caused by the difference in circulation distribution obtained from the BEM compared to the experimental one. When using the experimental circulation distribution, the discrepancies between the STM and the experimental velocity data are reduced, especially

for the negative thrust case, where the difference between the BEM and the experimental circulation distribution was significant. The remaining differences between the STM and the experimental values when considering the experimental circulation distribution originate from viscous phenomena that occur most at the tip and root part of the blade.

For the wing modeling, both the 2D and 3D image vortex techniques are validated separately using higher-order numerical simulations (RANS). This vortex image technique seems to accurately predict the spanwise lift distribution on a wing submerged in a jet. The numerical implementation also allows for the modeling of realistic nonuniform velocity profiles in the slipstream. Combining all the separate models allows for the iterative process of calculating the mutual aerodynamic interaction between the propeller and wing. There is a good match in the spanwise distribution of sectional lift between the VLM and experimental data for the tip-mounted propeller system. Using these improved models, a first-order estimation of the change in both propeller and wing performance can be calculated in a fast and accurate manner. In this way, the preliminary conceptual design of new aircraft, featuring distributed propellers, can be improved. This can aid in making aviation more sustainable and environmentally friendly.

Acknowledgments

Appendix A: Detailed STM Derivations

Analytically integrating the Biot–Savart law in the slipstream tube model for both the axial and tangential vorticity elements in the streamwise direction decreases the computational cost of the complete vortex system significantly. Furthermore, it avoids the possible numerical error introduced by the proximity of the streamwise tube coordinates with respect to the wing control points. However, the Biot–Savart law can only be easily integrated in this direction if the vortex strengths and the tube geometry are not a function of the streamwise coordinate. In other words, contraction or deformation of the slipstream vortex system is not taken into account.

A.1. Tangential Vorticity

The induced velocity in point Q due to this tangential vortex filament of length dl at radial position r and strength Γ_t (Fig. 6a) is given by

$$dV_Q = \frac{\Gamma_t(r)}{4\pi} \frac{dl \times r_Q}{|r_Q|^3} \tag{A1}$$

The strength of the tangential vorticity elements was described before. The vector along the length of the vortex filament (dl) can be expressed using the propeller cylindrical coordinates (r and φ):

$$dl = dl e_\varphi = rd\varphi e_\varphi \tag{A2}$$

where the circumferential unit vector e_φ can be represented in the Cartesian coordinate system as

$$e_\varphi = \begin{bmatrix} 0 \\ \cos(\varphi) \\ -\sin(\varphi) \end{bmatrix} \begin{matrix} i \\ j \\ k \end{matrix} \tag{A3}$$

So the position vector r_Q of control point Q with respect to the vorticity filament becomes

$$r_Q = \begin{bmatrix} x_Q - x \\ y_Q - y \\ z_Q - z \end{bmatrix} = \begin{bmatrix} x_Q - x \\ y_Q - r\sin(\varphi) \\ z_Q - r\cos(\varphi) \end{bmatrix} = \begin{bmatrix} x_Q - x \\ b \\ c \end{bmatrix} \begin{matrix} i \\ j \\ k \end{matrix} \tag{A4}$$

The norm of the position vector can be written as

$$|r_Q| = \sqrt{(x_Q - x)^2 + (y_Q - r\sin(\varphi))^2 + (z_Q - r\cos(\varphi))^2}$$
$$= \sqrt{(x_Q - x)^2 + b^2 + c^2} \tag{A5}$$

Below, Eq. (A1) is worked out for the tangential vorticity rings, starting with the cross product first:

$$dl \times r_Q = rd\varphi e_\varphi \times r_Q = rd\varphi \begin{bmatrix} 0 \\ \cos(\varphi) \\ -\sin(\varphi) \end{bmatrix} \times \begin{bmatrix} x_Q - x \\ b \\ c \end{bmatrix}$$
$$= rd\varphi \begin{bmatrix} \cos(\varphi)c + \sin(\varphi)b \\ -\sin(\varphi)(x_Q - x) \\ -\cos(\varphi)(x_Q - x) \end{bmatrix} \begin{matrix} i \\ j \\ k \end{matrix} \tag{A6}$$

Filling in the worked-out cross product in Eq. (A1) will lead to

$$dV_Q = \frac{\Gamma_t}{4\pi} \frac{rd\varphi}{((x_Q - x)^2 + b^2 + c^2)^{3/2}} \begin{bmatrix} c\cos(\varphi) + b\sin(\varphi) \\ -(x_Q - x)\sin(\varphi) \\ -(x_Q - x)\cos(\varphi) \end{bmatrix} \begin{matrix} i \\ j \\ k \end{matrix} \tag{A7}$$

To find the total induced axial velocity in point Q by the complete slipstream tube, the contribution of all tangential vorticity filaments needs to be integrated over all three dimensions in the cylindrical coordinate system (r, φ, and x):

$$V_Q = \int_{r=0}^{R} \int_{\varphi=0}^{2\pi} \int_{x=0}^{\infty} dV_Q$$
$$= \int_{r=0}^{R} \int_{\varphi=0}^{2\pi} \int_{x=0}^{\infty} \frac{nB}{4\pi V_\infty} \frac{d\Gamma_p}{dr} \frac{(1-a')}{(1+a)} \frac{r}{((x_Q - x)^2 + b^2 + c^2)^{3/2}}$$
$$\times \begin{bmatrix} c\cos(\varphi) + b\sin(\varphi) \\ -(x_Q - x)\sin(\varphi) \\ -(x_Q - x)\cos(\varphi) \end{bmatrix} dx\, d\varphi\, dr \tag{A8}$$

For clarity, the three velocity components of V_Q will be analyzed separately. As mentioned in Sec. III.B, the assumption of constant tube size along the streamwise coordinate and hence no contraction means that Eq. (A8) can be solved analytically in x:

$$V_{Q,x} = \int\limits_{r=0}^{R} \int\limits_{\varphi=0}^{2\pi} \int\limits_{x=0}^{\infty} dV_{Q,x} = \int\limits_{r=0}^{R} \int\limits_{\varphi=0}^{2\pi} \frac{nB}{4\pi V_\infty} \frac{d\Gamma_p}{dr} \frac{(1-a')}{(1+a)} r$$

$$\times \int\limits_{x=0}^{\infty} \frac{c\cos(\varphi)+b\sin(\varphi)}{((x_Q-x)^2+b^2+c^2)^{3/2}} \, dx \, d\varphi \, dr$$

$$= \int\limits_{r=0}^{R} \int\limits_{\varphi=0}^{2\pi} \frac{nB}{4\pi V_\infty} \frac{d\Gamma_p}{dr} \frac{(1-a')}{(1+a)} r$$

$$\times \left(-\frac{x_Q-x}{b^2+c^2} \frac{c\cos(\varphi)+b\sin(\varphi)}{\sqrt{(x_Q-x)^2+b^2+c^2}} \right)\Bigg|_0^\infty d\varphi \, dr$$

$$= \int\limits_{r=0}^{R} \int\limits_{\varphi=0}^{2\pi} \frac{nB}{4\pi V_\infty} \frac{d\Gamma_p}{dr} \frac{(1-a')}{(1+a)} r$$

$$\times \left(\frac{c\cos(\varphi)+b\sin(\varphi)}{b^2+c^2} \left(1 + \frac{x_Q}{\sqrt{x_Q^2+b^2+c^2}} \right) \right) d\varphi \, dr \tag{A9}$$

The worked-out integrals for $V_{Q,y}$ and $V_{Q,z}$ are slightly easier:

$$V_{Q,y} = \int\limits_{r=0}^{R} \int\limits_{\varphi=0}^{2\pi} \int\limits_{x=0}^{\infty} dV_{Q,y} = \int\limits_{r=0}^{R} \int\limits_{\varphi=0}^{2\pi} \frac{nB}{4\pi V_\infty} \frac{d\Gamma_p}{dr} \frac{(1-a')}{(1+a)} r$$

$$\times \int\limits_{x=0}^{\infty} \frac{-(x_Q-x)\sin(\varphi)}{((x_Q-x)^2+b^2+c^2)^{3/2}} \, dx \, d\varphi \, dr$$

$$= \int\limits_{r=0}^{R} \int\limits_{\varphi=0}^{2\pi} \frac{nB}{4\pi V_\infty} \frac{d\Gamma_p}{dr} \frac{(1-a')}{(1+a)} r$$

$$\times \left(-\frac{\sin(\varphi)}{\sqrt{(x_Q-x)^2+b^2+c^2}} \right)\Bigg|_0^\infty d\varphi \, dr$$

$$= \int\limits_{r=0}^{\infty} \int\limits_{\varphi=0}^{2\pi} \frac{nB}{4\pi V_\infty} \frac{d\Gamma_p}{dr} \frac{(1-a')}{(1+a)} r \left(\frac{\sin(\varphi)}{\sqrt{x_Q^2+b^2+c^2}} \right) d\varphi \, dr \tag{A10}$$

$$V_{Q,z} = \int\limits_{r=0}^{R} \int\limits_{\varphi=0}^{2\pi} \int\limits_{x=0}^{\infty} dV_{Q,z} = \int\limits_{r=0}^{R} \int\limits_{\varphi=0}^{2\pi} \frac{nB}{4\pi V_\infty} \frac{d\Gamma_p}{dr} \frac{(1-a')}{(1+a)} r$$

$$\times \int\limits_{x=0}^{\infty} \frac{-(x_Q-x)\cos(\varphi)}{((x_Q-x)^2+b^2+c^2)^{3/2}} \, dx \, d\varphi \, dr$$

$$= \int\limits_{r=0}^{R} \int\limits_{\varphi=0}^{2\pi} \frac{nB}{4\pi V_\infty} \frac{d\Gamma_p}{dr} \frac{(1-a')}{(1+a)} r$$

$$\times \left(-\frac{\cos(\varphi)}{\sqrt{(x_Q-x)^2+b^2+c^2}} \right)\Bigg|_0^\infty d\varphi \, dr$$

$$= \int\limits_{r=0}^{\infty} \int\limits_{\varphi=0}^{2\pi} \frac{nB}{4\pi V_\infty} \frac{d\Gamma_p}{dr} \frac{(1-a')}{(1+a)} r \left(\frac{\cos(\varphi)}{\sqrt{x_Q^2+b^2+c^2}} \right) d\varphi \, dr \tag{A11}$$

The other two integrals need to be worked out numerically for the three velocity components. This was presented in Sec. III.B.

A.2. Axial Vorticity

The induced velocity in point Q due to this axial vortex filament of length dl at radial position r and strength Γ_a (Fig. 6b) is given by

$$dV_Q = \frac{\Gamma_a(r)}{4\pi} \frac{dl \times r_Q}{|r_Q|^3} \tag{A12}$$

The vector along the vortex filament (dl) can be expressed directly in the Cartesian coordinate system:

$$dl = dl e_x = dx e_x \tag{A13}$$

Working out the cross product,

$$dl \times r_Q = dx e_x \times r_Q = dx \begin{bmatrix} -1 \\ 0 \\ 0 \end{bmatrix} \times \begin{bmatrix} x_Q-x \\ b \\ c \end{bmatrix} = dx \begin{bmatrix} 0 \\ c \\ -b \end{bmatrix} \begin{matrix} i \\ j \\ k \end{matrix} \tag{A14}$$

Filling in the worked-out cross product in Eq. (12) will lead to

$$dV_Q = \frac{\Gamma_a}{4\pi} \frac{dx}{((x_Q-x)^2+b^2+c^2)^{3/2}} \begin{bmatrix} 0 \\ c \\ -b \end{bmatrix} \begin{matrix} i \\ j \\ k \end{matrix} \tag{A15}$$

Working out the full integral,

$$V_Q = \int\limits_{r=0}^{R} \int\limits_{\varphi=0}^{2\pi} \int\limits_{x=0}^{\infty} dV_Q = \int\limits_{r=0}^{R} \int\limits_{\varphi=0}^{2\pi} \int\limits_{x=0}^{\infty} \frac{B}{8\pi^2} \frac{d\Gamma_p}{dr} \frac{1}{((x_Q-x)^2+b^2+c^2)^{3/2}}$$

$$\times \begin{bmatrix} 0 \\ c \\ -b \end{bmatrix} dx \, d\varphi \, dr \tag{A16}$$

Again, the integral in x-direction can be solved analytically for the three velocity components separately:

$$V_{Q,x} = 0 \tag{A17}$$

$$V_{Q,y} = \int\limits_{r=0}^{R} \int\limits_{\varphi=0}^{2\pi} \int\limits_{x=0}^{\infty} dV_{Q,y}$$

$$= \int\limits_{r=0}^{R} \int\limits_{\varphi=0}^{2\pi} \frac{B}{8\pi^2} \frac{d\Gamma_p}{dr} \int\limits_{x=0}^{\infty} \frac{c}{((x_Q-x)^2+b^2+c^2)^{3/2}} \, dx \, d\varphi \, dr$$

$$= \int\limits_{r=0}^{R} \int\limits_{\varphi=0}^{2\pi} \frac{B}{8\pi^2} \frac{d\Gamma_p}{dr} \left(\frac{-c(x_Q-x)}{(b^2+c^2)\sqrt{(x_Q-x)^2+b^2+c^2}} \right)\Bigg|_0^\infty d\varphi \, dr$$

$$= \int\limits_{r=0}^{R} \int\limits_{\varphi=0}^{2\pi} \frac{B}{8\pi^2} \frac{d\Gamma_p}{dr} \left(\frac{c}{b^2+c^2} \left(1 + \frac{x_Q}{\sqrt{x_Q^2+b^2+c^2}} \right) \right) d\varphi \, dr \tag{A18}$$

$$
\begin{aligned}
V_{Q,z} &= \int_{r=0}^{R} \int_{\varphi=0}^{2\pi} \int_{x=0}^{\infty} dV_{Q,z} \\
&= \int_{r=0}^{R} \int_{\varphi=0}^{2\pi} \frac{B}{8\pi^2} \frac{d\Gamma_{\mathrm{p}}}{dr} \int_{x=0}^{\infty} \frac{-b}{((x_Q - x)^2 + b^2 + c^2)^{3/2}} \, dx \, d\varphi \, dr \\
&= \int_{r=0}^{R} \int_{\varphi=0}^{2\pi} \frac{B}{8\pi^2} \frac{d\Gamma_{\mathrm{p}}}{dr} \left(\frac{b(x_Q - x)}{(b^2 + c^2)\sqrt{(x_Q - x)^2 + b^2 + c^2}} \right) \Bigg|_{0}^{\infty} d\varphi \, dr \\
&= \int_{r=0}^{R} \int_{\varphi=0}^{2\pi} \frac{B}{8\pi^2} \frac{d\Gamma_{\mathrm{p}}}{dr} \left(\frac{-b}{b^2 + c^2} \left(1 + \frac{x_Q}{\sqrt{x_Q^2 + b^2 + c^2}} \right) \right) d\varphi \, dr
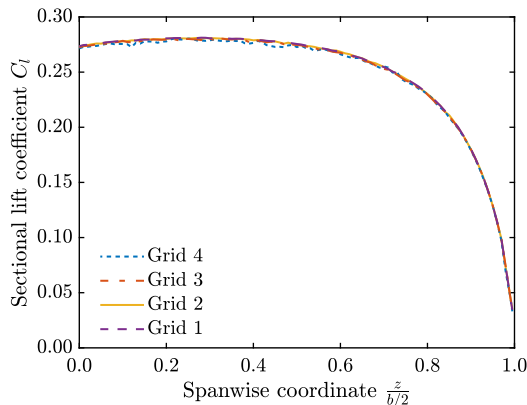\end{aligned}
$$

$$(A19)$$

Appendix B: Grid Dependence Study for RANS Simulations

The grid was refined systematically for the grid convergence study, except for the inflation layer, as per the recommendation of starting the grid convergence study from the edge of the wall layer out by Roache [83]. Following the methodology of Stokkermans et al. [76], the least-squares version of the grid convergence index proposed by Eça and Hoekstra [84] was used to estimate discretization error. Table B1 lists the grid sizes and refinement ratios h_i/h_1 for the studied configurations, where h_i is the average cell size of the grid i and h_1 represents the average cell size of the finest grid. Four different grids were used for the grid convergence study, with grid 4 being the coarsest and grid 1 the finest.
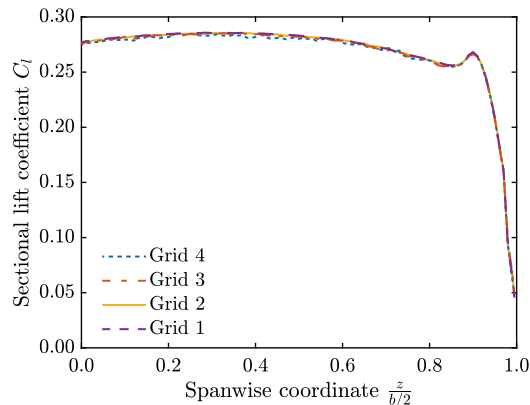
The systematic grid convergence analysis focused on the integrated lift coefficients for both the isolated wing and the wing with propeller cases, as the lift is the most relevant parameter for this study. The integrated lift coefficients obtained from different grids are listed in Table B1. For both cases, the estimated error in uncertainty ($|U_\phi|$) was calculated to be less than 1% (based on grid 2), indicating sufficient

grid resolution. Figure B1 compares lift coefficient distributions along the wingspan for different grids. For both the isolated wing as well as the installed propeller–wing configurations, lift distributions obtained from different grids show negligible differences. While the improvement in lift prediction between grids 2 and 1 is minimal, the computational cost increase is significant. Therefore, grid 2 was determined to be the most suitable in terms of the tradeoff between computational cost and solution refinement and was used for comparison with other models in this paper.

References

[1] Stoll, A. M., Bevirt, J., Moore, M. D., Fredericks, W. J., and Borer, N. K., "Drag Reduction Through Distributed Electric Propulsion," *14th AIAA Aviation Technology, Integration, and Operations Conference*, AIAA Paper 2014-2851, 2014,
https://doi.org/10.2514/6.2014-2851

[2] Borer, N. K., Patterson, M. D., Viken, J. K., Moore, M. D., Clarke, S., Redifer, M. E., Christie, R. J., Stoll, A. M., Dubois, A., Bevirt, J., et al., "Design and Performance of the NASA SCEPTOR Distributed Electric Propulsion Flight Demonstrator," *16th AIAA Aviation Technology, Integration, and Operations Conference*, AIAA Paper 2016-3920, 2016,
https://doi.org/10.2514/6.2016-3920

[3] "Elevating the Future of Air Mobility," Electra Aero, 2024, https://www.electra.aero.

[4] Prandtl, L., "Mutual Influence of Wings and Propeller," NACA TN-74, 1921, https://ntrs.nasa.gov/api/citations/19930080882/downloads/19930080882.pdf

[5] Snyder, M. H., and Zumwalt, G. W., "Effects of Wingtip-Mounted Propellers on Wing Lift and Induced Drag," *Journal of Aircraft*, Vol. 6, No. 5, 1969, pp. 392–397.
https://doi.org/10.2514/3.44076

[6] Witkowski, D. P., Lee, A. K. H., and Sullivan, J. P., "Aerodynamic Interaction Between Propellers and Wings," *Journal of Aircraft*, Vol. 26, No. 9, 1989, pp. 829–836.
https://doi.org/10.2514/3.45848

[7] Veldhuis, L. L. M., "Propeller Wing Aerodynamic Interference," Ph.D. Thesis, Faculty of Aerospace Engineering, Delft Univ. of Technology, Delft, The Netherlands, 2005, https://repository.tudelft.nl/islandora/object/uuid%3A8ffbde9c-b483-40de-90e0-97095202fbe3.

[8] Patterson, J. C., Jr., and Bartlett, G. R., "Evaluation of Installed Performance of a Wing-Tip-Mounted Pusher Turboprop on a Semispan Wing," NASA TP-2739, 1987, https://ntrs.nasa.gov/api/citations/19870016608/downloads/19870016608.pdf.

[9] Sinnige, T., van Arnhem, N., Stokkermans, T. C. A., Eitelberg, G., and Veldhuis, L. L. M., "Wingtip-Mounted Propellers: Aerodynamic Analysis of Interaction Effects and Comparison with Conventional Layout," *Journal of Aircraft*, Vol. 56, No. 1, 2019, pp. 295–312.
https://doi.org/10.2514/1.C034978

[10] Sinnige, T., Nederlof, R., and van Arnhem, N., "Aerodynamic Performance of Wingtip-Mounted Propellers in Tractor and Pusher Configuration," *AIAA Aviation Forum*, AIAA Paper 2021-2511, 2021.
https://doi.org/10.2514/6.2021-2511

[11] Hooker, J. R., Wick, A. T., Walker, J., and Schiltgen, B. T., "Overview of Low Speed Wind Tunnel Testing Conducted on a Wingtip Mounted Propeller for the Workshop for Integrated Propeller Prediction," *AIAA*

Table B1   Grid convergence study of RANS simulations.

Grid	No. of cells	h_i/h_1	$C_{L_{\mathrm{iso}}}$	C_{L_p}
4	7,986,317	1.62	0.2542	0.2712
3	11,469,347	1.44	0.2551	0.2720
2	16,013,202	1.28	0.2558	0.2728
1	33,921,269	1.00	0.2560	0.2730
Discretization error $|U_\phi|$ (based on grid 2)			0.95%	0.87%

a) Clean-wing configuration

b) Installed propeller-wing configuration

Fig. B1   Comparison of the sectional lift distributions for the clean-wing and the propeller–wing system for different grids.

Aviation Forum, AIAA Paper 2020-2673, 2020.
https://doi.org/10.2514/6.2020-2673

[12] Pfeifle, O., Notter, S., Fichter, W., Bergmann, D. P., Denzel, J., and Strohmayer, A., "Verifying the Effect of Wingtip Propellers on Drag Through In-Flight Measurements," *Journal of Aircraft*, Vol. 59, No. 2, 2022, pp. 474–483.
https://doi.org/10.2514/1.C036490

[13] van Arnhem, N., Sinnige, T., Stokkermans, T. C. A., Eitelberg, G., and Veldhuis, L. L. M., "Aerodynamic Interaction Effects of Tip-Mounted Propellers Installed On the Horizontal Tailplane," *AIAA Aerospace Sciences Meeting*, AIAA Paper 2018-2052, 2018.
https://doi.org/10.2514/6.2018-2052

[14] van Arnhem, N., de Vries, R., Sinnige, T., Vos, R., and Veldhuis, L. L. M., "Aerodynamic Performance and Static Stability Characteristics of Aircraft with Tail-Mounted Propellers," *Journal of Aircraft*, Vol. 59, No. 2, 2022, pp. 415–432.
https://doi.org/10.2514/1.C036338

[15] Stokkermans, T. C. A., Usai, D., Sinnige, T., and Veldhuis, L. L. M., "Aerodynamic Interaction Effects Between Propellers in Typical eVTOL Vehicle Configurations," *Journal of Aircraft*, Vol. 58, No. 4, 2021, pp. 815–833.
https://doi.org/10.2514/1.C035814

[16] Kroo, I., "Propeller-Wing Integration for Minimum Induced Loss," *Journal of Aircraft*, Vol. 23, No. 7, 1986, pp. 561–565.
https://doi.org/10.2514/3.45344

[17] Miranda, L. R., and Brennan, J. E., "Aerodynamic Effects of Wingtip-Mounted Propellers and Turbines," *4th Applied Aerodynamics Conference*, AIAA Paper 1986-1802, 1986.
https://doi.org/10.2514/6.1986-1802

[18] Chauhan, S. S., and Martins, J. R. R. A., "RANS-Based Aerodynamic Shape Optimization of a Wing Considering Propeller–Wing Interaction," *Journal of Aircraft*, Vol. 58, No. 3, 2021, pp. 497–513.
https://doi.org/10.2514/1.C035991

[19] Taniguchi, S., and Oyama, A., "Numerical Analysis of Propeller Mounting Position Effects on Aerodynamic Propeller/Wing Interaction," *AIAA SciTech Forum*, AIAA Paper 2022-0153, 2022.
https://doi.org/10.2514/6.2022-0153

[20] Keller, D., "Towards Higher Aerodynamic Efficiency of Propeller-Driven Aircraft with Distributed Propulsion," *CEAS Aeronautical Journal*, Vol. 12, No. 4, 2021, pp. 777–791.
https://doi.org/10.1007/s13272-021-00535-5

[21] Zhou, B. Y., Gauger, N. R., Morelli, M., and Guardone, A., "Simulation and Sensitivity Analysis of a Wing-Tip Mounted Propeller Configuration From the Workshop for Integrated Propeller Prediction (WIPP)," *AIAA Aviation Forum*, AIAA Paper 2020-2683, 2020.
https://doi.org/10.2514/6.2020-2683

[22] Aref, P., Ghoreyshi, M., Jirasek, A., Satchell, M. J., and Bergeron, K., "Computational Study of Propeller Wing Aerodynamic Interaction," *AIAA Aerospace Sciences Meeting*, AIAA Paper 2018-0778, 2018.
https://doi.org/10.2514/6.2018-0778

[23] Patterson, M. D., Daskilewicz, M. J., and German, B. J., "Conceptual Design of Electric Aircraft with Distributed Propellers: Multidisciplinary Analysis Needs and Aerodynamic Modeling Development," *52nd Aerospace Sciences Meeting*, AIAA Paper 2014-0534, 2014.
https://doi.org/10.2514/6.2014-0534

[24] de Vries, R., Brown, M., and Vos, R., "Preliminary Sizing Method for Hybrid-Electric Distributed-Propulsion Aircraft," *Journal of Aircraft*, Vol. 56, No. 6, 2019, pp. 2172–2188.
https://doi.org/10.2514/1.C035388

[25] Hoogreef, M. F. M., de Vries, R., Sinnige, T., and Vos, R., "Synthesis of Aero-Propulsive Interaction Studies Applied to Conceptual Hybrid-Electric Aircraft Design," *AIAA SciTech Forum*, AIAA Paper 2020-0503, 2020.
https://doi.org/10.2514/6.2020-0503

[26] Stone, R. H., "Aerodynamic Modeling of the Wing-Propeller Interaction for a Tail-Sitter Unmanned Air Vehicle," *Journal of Aircraft*, Vol. 45, No. 1, 2008, pp. 198–210.
https://doi.org/10.2514/1.15705

[27] Erhard, R. M., Clarke, M. A., and Alonso, J. J., "A Low-Cost Aero-Propulsive Analysis of Distributed Electric Propulsion Aircraft," *AIAA SciTech Forum*, AIAA Paper 2021-1200, 2021.
https://doi.org/10.2514/6.2021-1200

[28] Cole, J. A., Krebs, T., Barcelos, D., and Bramesfeld, G., "Influence of Propeller Location, Diameter, and Rotation Direction on Aerodynamic Efficiency," *Journal of Aircraft*, Vol. 58, No. 1, 2021, pp. 63–71.
https://doi.org/10.2514/1.C035917

[29] Cole, J. A., Maughmer, M. D., Kinzel, M., and Bramesfeld, G., "High-Order Free-Wake Method for Propeller-Wing Systems," *Journal of*

Aircraft, Vol. 56, No. 1, 2019, pp. 150–165.
https://doi.org/10.2514/1.C034720

[30] Alvarez, E. J., and Ning, A., "Meshless Large-Eddy Simulation of Propeller–Wing Interactions with Reformulated Vortex Particle Method," *Journal of Aircraft*, Vol. 61, No. 3, 2024, pp. 811–827.
https://doi.org/10.2514/1.C037279

[31] Ahuja, V., and Hartfield, R. J., "Predicting the Aero Loads Behind a Propeller in the Presence of a Wing Using Flightstream," *15th AIAA Aviation Technology, Integration, and Operations Conference*, AIAA Paper 2015-2734, 2015.
https://doi.org/10.2514/6.2015-2734

[32] Clarke, M. A., Erhard, R. M., and Alonso, J. J., "Aerodynamic Optimization of Wing-Mounted Propeller Configurations for Distributed Electric Propulsion Architectures," *AIAA Aviation Forum*, AIAA Paper 2021-2471, 2021.
https://doi.org/10.2514/6.2021-2471

[33] D'Angelo, B., Balachandran, H. K., and Gopalarathnam, A., "Low-Order and Computational Modeling of Propeller-Wing Interactions," *AIAA Aviation Forum*, AIAA Paper 2022-3686, 2022.
https://doi.org/10.2514/6.2022-3686

[34] Hunsaker, D., and Snyder, D., "A Lifting-Line Approach to Estimating Propeller/Wing Interactions," *24th AIAA Applied Aerodynamics Conference*, AIAA Paper 2006-3466, 2006.
https://doi.org/10.2514/6.2006-3466

[35] Comunian, P., Serpieri, J., and Cafiero, G., "A Genetic-Algorithm Based Approach for Optimized Distributed Electric Propulsion," *AIAA Aviation Forum and ASCEND*, AIAA Paper 2024-3603, 2024.
https://doi.org/10.2514/6.2024-3603

[36] McVeigh, M. A., Gray, L., and Kisielowski, E., "Prediction of Span Loading of Straight-Wing/Propeller Combinations Up to Stall," NASA CR-2602, 1975, https://ntrs.nasa.gov/api/citations/19760004918/downloads/19760004918.pdf.

[37] Shollenberger, C. A., "Three-Dimensional Wing/Jet Interaction Analysis Including Jet Distortion Influences," *Journal of Aircraft*, Vol. 12, No. 9, 1975, pp. 706–713.
https://doi.org/10.2514/3.59862

[38] Ting, L., and Liu, C. H., "Thin Airfoil in Nonuniform Parallel Stream," *Journal of Aircraft*, Vol. 6, No. 2, 1969, pp. 173–175.
https://doi.org/10.2514/3.44030

[39] Prabhu, R. K., "Studies On the Interference of Wings and Propeller Slipstreams," Ph.D. Thesis, Old Dominion Univ., Norfolk, VA, 1984, https://doi.org/10.25777/ezag-d204

[40] Patterson, M. D., and German, B. J., "Simplified Aerodynamics Models to Predict the Effects of Upstream Propellers on Wing Lift," *53rd AIAA Aerospace Sciences Meeting*, AIAA Paper 2015-1673, 2015.
https://doi.org/10.2514/6.2015-1673

[41] Patterson, M. D., Derlaga, J. M., and Borer, N. K., "High-Lift Propeller System Configuration Selection for NASA's SCEPTOR Distributed Electric Propulsion Flight Demonstrator," *16th AIAA Aviation Technology, Integration, and Operations Conference*, AIAA Paper 2016-3922, 2016.
https://doi.org/10.2514/6.2016-3922

[42] Ting, L., Liu, C. H., and Kleinstein, G., "Interference of Wing and Multipropellers," *AIAA Journal*, Vol. 10, No. 7, 1972, pp. 906–914.
https://doi.org/10.2514/3.50244

[43] Rethorst, S., "Aerodynamic of Nonuniform Flows as Related to an Airfoil Extending Through a Circular Jet," *Journal of the Aerospace Sciences*, Vol. 25, No. 1, 1958, pp. 11–28.
https://doi.org/10.2514/8.7479

[44] Gur, O., and Rosen, A., "Comparison Between Blade-Element Models of Propellers," *The Aeronautical Journal*, Vol. 112, No. 1138, 2008, pp. 689–704.
https://doi.org/10.1017/S0001924000002669

[45] McCrink, M. H., and Gregory, J. W., "Blade Element Momentum Modeling of Low-Reynolds Electric Propulsion Systems," *Journal of Aircraft*, Vol. 54, No. 1, 2017, pp. 163–176.
https://doi.org/10.2514/1.C033622

[46] Barnes, J. P., "Hybrid Lifting-Line/Blade-Element Method for Propeller or Propfan Performance," *35th AIAA Applied Aerodynamics Conference*, AIAA Paper 2017-3570, 2017.
https://doi.org/10.2514/6.2017-3570

[47] Goyal, J., Sinnige, T., Avallone, F., and Ferreira, C., "Benchmarking of Aerodynamic Models for Isolated Propellers Operating at Positive and Negative Thrust," *AIAA Journal*, Vol. 62, No. 10, 2024, pp. 3758–3775.
https://doi.org/10.2514/1.J064093

[48] Rwigema, M. K., "Propeller Blade Element Momentum Theory with Vortex Wake Deflection," *27th International Congress of the Aeronaut-*

ical Sciences, ICAS Paper 2010-434, 2010, https://www.icas.org/ICAS_ARCHIVE/ICAS2010/PAPERS/434.PDF.

[49] Goyal, J., "Blade Element Momentum Theory for Positive and Negative Thrust Propellers, *4TU, ResearchData, Software*, 2023. https://doi.org/10.4121/e748a68d-5f15-4757-b904-880bcec8217b

[50] Van Rooij, R. P. J. O. M., "Modification of the Boundary Layer Calculation in RFOIL for Improved Airfoil Stall Prediction," Report IW-96087R, Delft Univ. of Technology, Delft, The Netherlands, 1996, https://www.osti.gov/etdeweb/biblio/20102159.

[51] Drela, M., "XFOIL: An Analysis and Design System for Low Reynolds Number Airfoils," *Low Reynolds Number Aerodynamics. Lecture Notes in Engineering*. Vol. 54, Springer, Berlin, 1989. https://doi.org/10.1007/978-3-642-84010-4_1

[52] Park, S., "Blade Element Momentum Method for Propeller Under Non-axial Flow," *International Journal of Aeronautical and Space Sciences*, Vol. 24, No. 2, 2022, pp. 334–340. https://doi.org/10.1007/s42405-022-00535-7

[53] Leng, Y., Yoo, H., Jardin, T., Bronz, M., and Moschetta, J., "Aerodynamic Modelling of Propeller Forces and Moments at High Angle of Incidence," *AIAA SciTech Forum*, AIAA Paper 2019-1332, 2019. https://doi.org/10.2514/6.2019-1332

[54] van Arnhem, N., de Vries, R., Sinnige, T., Vos, R., Eitelberg, G., and Veldhuis, L. L. M., "Engineering Method to Estimate the Blade Loading of Propellers in Nonuniform Flow," *AIAA Journal*, Vol. 28, No. 12, 2020, pp. 5332–5346. https://doi.org/10.2514/1.J059485

[55] Goyal, J., Sinnige, T., Ferreira, C., and Avallone, F., "Aerodynamics and Far-Field Noise Emissions of a Propeller in Positive and Negative Thrust Regimes at Non-Zero Angles of Attack," *AIAA Aviation Forum*, AIAA Paper 2023-3217, 2023. https://doi.org/10.2514/6.2023-3217

[56] Metcalfe, M. P., "On the Modelling of a Fully-Relaxed Propeller Slip-stream," *21st Joint Propulsion Conference*, AIAA Paper 1985-1262, 1985. https://doi.org/10.2514/6.1985-1262

[57] Otsuka, K., del Carre, A., and Palacios, R., "Nonlinear Aeroelastic Analysis of High-Aspect-Ratio Wings with a Low-Order Propeller Model," *Journal of Aircraft*, Vol. 59, No. 2, 2022, pp. 293–306. https://doi.org/10.2514/1.C036285

[58] Weissinger, J., "The Lift Distribution of Swept-Back Wings," NACA TM-1120, 1947, https://ntrs.nasa.gov/api/citations/20030064148/downloads/20030064148.pdf.

[59] Ewald, B. F. R. (ed.), *Wind Tunnel Wall Corrections*, AGARDograph 336, 1998, https://apps.dtic.mil/sti/tr/pdf/ADA356695.pdf.

[60] Nederlof, R., "Improved Modeling of Propeller-Wing Interactions with a Lifting-Line Approach: Investigation of a Suitable Correction Method to Account for the Finite Slipstream Height," M.Sc. Thesis, Delft Univ. of Technology, Delft, The Netherlands, 2020, https://repository.tudelft.nl/islandora/object/uuid%3Ad952665d-475f-483d-94f5-2b929ea6e713?collection=education.

[61] Phillips, W. F., and Snyder, D. O., "Modern Adaptation of Prandtl's Classic Lifting-Line Theory," *Journal of Aircraft*, Vol. 37, No. 4, 2000, pp. 662–670. https://doi.org/10.2514/2.2649

[62] Nederlof, R., Kooij, R., Veldhuis, L. L. M., and Sinnige, T., "Contribution of Swirl Recovery to the Induced Drag of a Propeller-Wing System – A Parametric Study," *AIAA Aviation Forum*, AIAA Paper 2023-3543, 2023. https://doi.org/10.2514/6.2023-3543

[63] Drela, M., and Youngren, H., "AVL 3.40 User Primer," 2022, https://web.mit.edu/drela/Public/web/avl/avl_doc.txt.

[64] Horsten, B., and Veldhuis, L. L. M., "A New Hybrid Method to Correct for Wind Tunnel Wall- and Support Interference On-Line," *World Academy of Science, Engineering and Technology*, Vol. 58, 2009, pp. 507–514. https://doi.org/10.5281/zenodo.1072187

[65] "MATLAB version: 23.2 (R2023b)," The MathWorks, Inc., 2023, https://www.mathworks.com.

[66] Nederlof, R., Ragni, D., and Sinnige, T., "Experimental Investigation of the Aerodynamic Performance of a Propeller at Positive and Negative Thrust and Power," *AIAA Aviation Forum*, AIAA Paper 2022-3893, 2022. https://doi.org/10.2514/6.2022-3893

[67] Nederlof, R., Ragni, D., and Sinnige, T., "Energy-Harvesting Performance of an Aircraft Propeller," *Journal of Aircraft*. https://doi.org/10.2514/1.C038005

[68] Nederlof, R., Ragni, D., and Sinnige, T., "TUD-XPROP-3 Propeller Geometry," *Zenodo*, 2024, https://doi.org/10.5281/zenodo.13645390

[69] Haans, W., van Kuijk, G., and van Bussel, G., "The Inverse Vortex Wake Model: A Measurement Analysis Tool," *ASME Journal of Solar Energy Engineering*, Vol. 130, No. 3, 2008, Paper 031009. https://doi.org/10.1115/1.2931508

[70] Van Zelst, P., "2D Modeling Approach for Propeller-Wing-Flap Interactions," M.Sc. Thesis, Delft Univ. of Technology, Delft, The Netherlands, 2021, http://resolver.tudelft.nl/uuid:c5c1c090-6cd2-4134-8575-3adaf4d6bb90.

[71] Drela, M., "A User's Guide to MSES 3.05," MIT Department of Aeronautics and Astronautics, 2007, https://web.mit.edu/drela/Public/web/mses/mses.pdf.

[72] Duivenvoorden, R. R., Sinnige, T., Veldhuis, L. L. M., and Friedrichs, J., "Multi-Element Airfoil in Jet Flows: Identifying Dominant Factors and Interactions," *Journal of Aircraft*, Vol. 61, No. 5, 2024, pp. 1517–1534. https://doi.org/10.2514/1.C037741

[73] Sinnige, T., and Della Corte, B., "Aerodynamic Performance of a Tip-Mounted Propeller-Wing System at Positive and Negative Thrust," *AIAA Aviation Forum and ASCEND*, AIAA Paper 2024-3520, 2024. https://doi.org/10.2514/6.2024-3520

[74] Sinnige, T., Goyal, T., Nederlof, R., Pagliaroli, T., Candeloro, P., Martellini, E., Kiran, A., Zaghari, B., Pontika, E., Balaghi Enalou, H., et al., "Deliverable 3.3: Energy Harvesting," European Commission TR Fut-PrInt50, 2023.

[75] Anon., "ANSYS® Academic Research Release 2019 R3 Help System, Fluent," ANSYS, Canonsburg, PA, 2019.

[76] Stokkermans, T. C. A., van Arnhem, N., Sinnige, T., and Veldhuis, L. L. M., "Validation and Comparison of RANS Propeller Modeling Methods for Tip-Mounted Applications," *AIAA Journal*, Vol. 57, No. 2, 2019, pp. 566–580. https://doi.org/10.2514/1.J057398

[77] Schollenberger, M., Kirsch, B., Lutz, T., Krämer, E., and Friedrichs, J., "Aerodynamic Interactions Between Distributed Propellers and the Wing of an Electric Commuter Aircraft at Cruise Conditions," *CEAS Aeronautical Journal*, Vol. 15, No. 2, 2024, pp. 255–267. https://doi.org/10.1007/s13272-023-00706-6

[78] Sathyandra Rao, K., Sivapragasam, M., Narahari, H. K., and Bharadwaj, A. V., "Aerodynamic Optimization of Transonic Wing for Light Jet Aircraft," *Design and Development of Aerospace Vehicles and Propulsion Systems*, edited by S. K. Kumar, I. Narayanaswamy, and V. Ramesh, Springer, Singapore, 2021, pp. 253–265, https://doi.org/10.1007/978-981-15-9601-8_19

[79] Garmann, D. J., and Visbal, M. R., "Streamwise-Oriented Vortex Interactions with a NACA0012 Wing," *53rd AIAA Aerospace Sciences Meeting*, AIAA Paper 2015-1066, 2015. https://doi.org/10.2514/6.2015-1066

[80] Visbal, R. M., and Garmann, D. J., "Dynamic Stall of a Finite-Aspect-Ratio Wing," *AIAA Journal*, Vol. 57, No. 3, 2019, pp. 962–977. https://doi.org/10.2514/1.J057457

[81] Spalart, P. R., and Allmaras, S. R., "A One-Equation Turbulence Model for Aerodynamic Flows," *30th Aerospace Sciences Meeting*, AIAA Paper 1992-439, June 1992. https://doi.org/10.2514/6.1992-439

[82] Dacles-Mariani, J., Zilliac, G. G., Chow, J. S., and Bradshaw, P., "Numerical/Experimental Study of a Wingtip Vortex in the Near Field," *AIAA Journal*, Vol. 33, No. 9, 1995, pp. 1561–1568. https://doi.org/10.2514/3.12826

[83] Roache, P. J., "Quantification of Uncertainty in Computational Fluid Dynamics," *Annual Review of Fluid Mechanics*, Vol. 29, No. 1, 1997, pp. 123–160. https://doi.org/10.1146/annurev.fluid.29.1.123

[84] Eça, L., and Hoekstra, M., "A Procedure for the Estimation of the Numerical Uncertainty of CFD Calculations Based on Grid Refinement Studies," *Journal of Computational Physics*, Vol. 262, 2014, pp. 104–130. https://doi.org/10.1016/j.jcp.2014.01.006

F. Coton
Associate Editor